

# 2

## Integral Equation Methods for Scattering from Infinite Cylinders

We begin our investigation of numerical techniques by considering two-dimensional scatterers illuminated by normally incident plane waves. This chapter considers formulations based on the electric and magnetic field integral equations (EFIE and MFIE, respectively). Although the problems considered and methods employed are relatively simple, they illustrate the approach to be followed in more complicated formulations. In addition, a goal of this chapter is the presentation of sufficient detail to enable the reader to implement these techniques in software. To demonstrate possible approaches, sample FORTRAN programs are described in the Appendices.

### 2.1 TM-WAVE SCATTERING FROM CONDUCTING CYLINDERS: EFIE DISCRETIZED WITH PULSE BASIS AND DELTA TESTING FUNCTIONS [1]

The cross section of an infinite, perfectly conducting (p.e.c.) cylinder is depicted in Figure 2.1. Using the surface equivalence principle from Section 1.6, the p.e.c. material may be replaced by equivalent electric currents radiating in free space. For a normally incident TM wave, the field components present are  $E_z$ ,  $H_x$ , and  $H_y$  and the only current component present is  $J_z$ . Since  $\nabla \cdot \vec{J} = 0$  for the TM polarization, which in turn implies that  $\nabla \cdot \vec{A} = 0$ , the EFIE from (1.96) can be specialized to

$$E_z^{\text{inc}}(t) = jk\eta A_z(t) \quad (2.1)$$

where

$$A_z(t) = \int J_z(t') \frac{1}{4j} H_0^{(2)}(kR) dt' \quad (2.2)$$

$$R = \sqrt{[x(t) - x(t')]^2 + [y(t) - y(t')]^2} \quad (2.3)$$

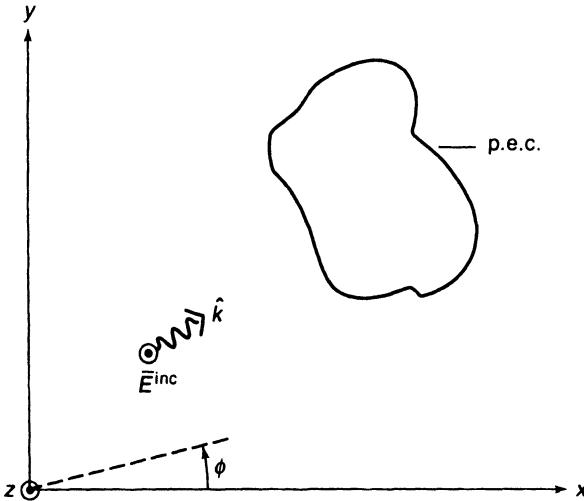


**Figure 2.1** A p.e.c. cylinder illuminated by an incident TM wave.

and  $t$  is a parametric variable denoting the position around the contour of the cylinder surface. Note that Equation (2.1) is only valid at points on the surface of the original cylinder.

To construct an approximate solution for  $J_z$ , we divide the cylinder contour into cells as illustrated in Figure 2.2. As a function of position around the contour, the equivalent current density can be approximated by the superposition of subsectional pulse basis functions

$$p_n(t) = \begin{cases} 1 & \text{if } t \in \text{cell } n \\ 0 & \text{otherwise} \end{cases} \quad (2.4)$$

so that

$$J_z(t) \cong \sum_{n=1}^N j_n p_n(t) \quad (2.5)$$

Substituting (2.5) into Equation (2.1) produces

$$E_z^{\text{inc}}(t) \cong jk\eta \sum_{n=1}^N j_n \int_{\text{cell } n} \frac{1}{4j} H_0^{(2)}(kR) dt' \quad (2.6)$$

This substitution replaces the original problem of finding  $J_z(t)$  with that of finding  $N$  unknown coefficients  $\{j_n\}$ . The  $N$  linearly independent equations may be obtained by enforcing Equation (2.6) at the centers of each of the  $N$  cells, to produce the  $N \times N$  system

$$\begin{bmatrix} E_z^{\text{inc}}(t_1) \\ E_z^{\text{inc}}(t_2) \\ \vdots \\ E_z^{\text{inc}}(t_N) \end{bmatrix} = \begin{bmatrix} Z_{11} & Z_{12} & \cdots & Z_{1N} \\ Z_{21} & Z_{22} & & Z_{2N} \\ \vdots & \vdots & & \vdots \\ Z_{N1} & Z_{N2} & \cdots & Z_{NN} \end{bmatrix} \begin{bmatrix} j_1 \\ j_2 \\ \vdots \\ j_N \end{bmatrix} \quad (2.7)$$

We say that Equation (2.1) has been *discretized* to form the matrix equation (2.7). The specific procedure we followed to convert the continuous integral equation to a discrete matrix equation is one form of a general approach known as the method of moments [1].

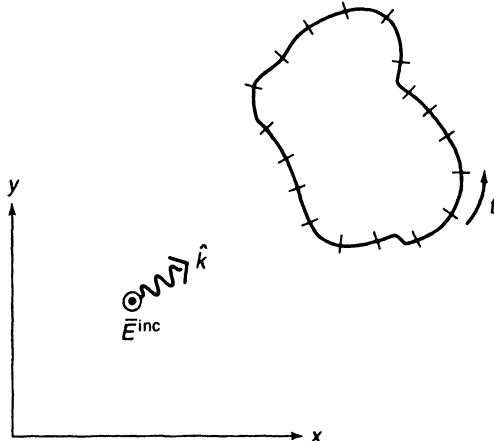


**Figure 2.2** Cylinder contour divided into cells.

This discretization procedure will be used throughout the text and will be discussed in more generality in Chapter 5. Once Equation (2.7) is constructed, it can be solved by standard algorithms (Chapter 4).

The  $N \times N$  matrix in Equation (2.7) is often called the *moment method impedance matrix* since its entries represent the mutual impedance between different cells in the model. For this example, these entries are given by

$$Z_{mn} = \frac{k\eta}{4} \int_{\text{cell } n} H_0^{(2)}(kR_m) dt' \quad (2.8)$$

where

$$R_m = \sqrt{[x_m - x(t')]^2 + [y_m - y(t')]^2} \quad (2.9)$$

and  $(x_m, y_m)$  represents the phase center of the  $m$ th strip in the model. Although the integral in Equation (2.8) cannot be evaluated exactly, if the cells are small compared to the wavelength, a possible approximation is [1]

$$Z_{mn} \approx \frac{k\eta}{4} w_n H_0^{(2)}(kR_{mn}) \quad m \neq n \quad (2.10)$$

where

$$R_{mn} = \sqrt{(x_m - x_n)^2 + (y_m - y_n)^2} \quad (2.11)$$

The diagonal elements of the impedance matrix cannot be approximated using Equation (2.10) because the Hankel function is singular (infinite) for  $R_{mn} = 0$ . In addition, it is usually important to accurately evaluate the diagonal impedance matrix entries, since they are relatively large and tend to give a greater contribution to the solution of the system. For small arguments, the Hankel function can be replaced by a power series expansion [2]

$$H_0^{(2)}(x) \approx \left( 1 - \frac{x^2}{4} \right) - j \left\{ \frac{2}{\pi} \ln \left( \frac{\gamma x}{2} \right) + \left[ \frac{1}{2\pi} - \frac{1}{2\pi} \ln \left( \frac{\gamma x}{2} \right) \right] x^2 \right\} + O(x^4) \quad (2.12)$$

where

$$\gamma = 1.781072418\dots \quad (2.13)$$

Assuming that the total curvature of each cell is small enough so that each cell may be considered flat, the dominant terms in Equation (2.12) can be retained to produce

$$\begin{aligned} \int_{\text{cell } m} H_0^{(2)}(kR_m) dt' &\cong 2 \int_0^{w_m/2} \left[ 1 - j \frac{2}{\pi} \ln \left( \frac{\gamma k u}{2} \right) \right] du \\ &= w_m - j \frac{2}{\pi} w_m \left[ \ln \left( \frac{\gamma k w_m}{4} \right) - 1 \right] \end{aligned} \quad (2.14)$$

It follows that

$$Z_{mm} \cong \frac{k\eta w_m}{4} \left\{ 1 - j \frac{2}{\pi} \left[ \ln \left( \frac{\gamma k w_m}{4} \right) - 1 \right] \right\} \quad (2.15)$$

The above approach will produce an approximate solution for the equivalent current density  $J_z$ . Once  $J_z$  is determined, secondary quantities of interest such as the bistatic scattering cross section  $\sigma_{\text{TM}}(\phi)$  can be computed. The calculation of scattering cross section for a two-dimensional cylinder geometry has been discussed in Chapter 1. If the incident field is of the form

$$E_z^{\text{inc}}(x, y) = e^{-jk(x \cos \phi^{\text{inc}} + y \sin \phi^{\text{inc}})} \quad (2.16)$$

Equation (1.138) can be specialized to this example to produce

$$\sigma_{\text{TM}}(\phi) \cong \frac{k\eta^2}{4} \left| \sum_{n=1}^N j_n w_n e^{jk(x_n \cos \phi + y_n \sin \phi)} \right|^2 \quad (2.17)$$

In order to implement the above procedure in software, two key issues must be addressed. The first concerns the data structure used to describe the scatterer model within the computer program. This information must unambiguously specify the model yet should be concise and relatively easy to access when required. The second issue concerns the particular algorithm used to evaluate the matrix elements. One possible approach for evaluating Equation (2.8) is suggested in the preceding discussion and leads to the approximate expressions in Equations (2.10) and (2.15). Employing these approximations for the matrix entries not only eliminates the need for some form of numerical quadrature but also greatly simplifies the modeling task. Specifically, the cylinder contour can be completely described by the coordinates of the phase center  $(x_n, y_n)$  of each cell and the width  $w_n$  of each cell. No additional information is required to construct Equation (2.7). It is interesting that no information about the orientation of each cell is incorporated into this model. Clearly, because of the approximations employed, there is a *resolution limit* inherent in the modeling. As a consequence, different physical scatterers may produce identical computer models. It is important not to expect accuracy beyond the resolution available for a given model.

Successful implementation of the numerical procedure hinges on the use of a meaningful scatterer model. Proper modeling is something of an art. The cell sizes in use must always be small compared to the wavelength  $\lambda_0$ , and a suggested maximum size is  $\lambda_0/10$ . Note that the approximation employed in Equation (2.14) for the diagonal matrix elements is based on a flat-cell assumption, which also may limit the cell size. The procedure based on Equations (2.10) and (2.15) has been found to give the best accuracy when the phase centers  $(x_n, y_n)$  of each cell are located on the surface of the original cylinder. In other words, rather than model the original contour with a polygon having the edges of each cell located on the original contour, it appears best to locate the cell centers on the original scatterer contour. In addition, the total circumference of the cylinder model should be scaled to equal that of the original scatterer contour. This scaling can be performed by modifying the widths  $\{w_n\}$  without changing the locations  $(x_n, y_n)$ . Despite the fact that the resulting scatterer model is slightly nonphysical, such a scaling appears to produce a more accurate current density.

For ease of use, it is convenient to organize general-purpose computational software packages into several distinct stages. The first stage, known as *preprocessing*, encompasses the generation of a suitable scatterer model. Depending on the specific geometry under consideration, this task may be highly automated (simple geometries) or may require many man-hours of human input and verification (complex geometries). As an aid to visualization, preprocessing often involves a color graphic display of the scatterer model. The end result of the preprocessing stage is a data file containing the model in a form that is directly compatible with the main analysis routines. The second stage of the process, *analysis*, primarily consists of the creation and solution of a matrix equation such as (2.7). The analysis stage is computationally intensive but requires little human input or effort. Specialized calculations such as the scattering cross section computation may also be performed in the analysis stage. The output from the analysis stage consists of all numerical results arranged in data files in some fashion that may not be particularly convenient for interpretation. These results are collected and reorganized in the *postprocessing stage*. Postprocessing may include the generation of graphs, contour plots, color pictures, and even color videos in order to permit the user to visualize and interpret the numerical results.

The preprocessing and postprocessing stages are generic to a wide variety of engineering applications and can be adapted from software packages that have no direct link to electromagnetic modeling. The analysis stage, however, must be developed for the specific electromagnetic scattering problem of interest. Therefore, we will emphasize the analysis stage of the numerical process throughout this text.

It is appropriate to consider the sources of error in the above analysis, and we propose the following classifications:

*Modeling errors:* errors introduced by replacing the actual geometry by the perfectly conducting, infinite cylinder; the precise location of the cell phase centers ( $x_n, y_n$ ); and the flat-strip model of the smooth-cylinder contour.

*Discretization errors:* errors due to the replacement of  $J_z(t)$  by the pulse expansion and the approximate enforcement of the integral equation only at the cell centers (an approach known as *point matching* [1]).

*Approximations:* errors introduced by the approximations employed to simplify the formulation, such as the “single-point” evaluation of the integral suggested in Equation (2.10).

*Numerical errors:* round-off errors such as those occurring in the calculation of the Bessel functions and the solution of the matrix equation.

Each type of error may dominate in a specific situation.

Relatively simple procedures were used to obtain the approximate expressions in (2.10) and (2.15) for the matrix elements. These approximations appear sensible, in the sense that as the cell sizes are reduced, the accuracy of the approximation improves. Note that the approximation used for the current density should also improve as the cell sizes are reduced, and thus we might expect the solution to converge to some limit as the model in question is refined (Prob. P2.2). These observations seem consistent with the general goal of this type of numerical analysis, which is to construct a solution in such a way that the accuracy improves as the cell sizes are reduced. However, since the cell sizes will never shrink to zero in practice, it may be necessary to improve the approximations in order to obtain good accuracy for a finite value of  $N$ . One way of accomplishing this is to accurately evaluate the matrix entries. The entries nearest the main diagonal often represent interactions between cells in close proximity, where (2.10) can be a poor approximation.

If a more accurate evaluation of Equation (2.8) is desired, numerical quadrature may be employed to evaluate the integrals to a somewhat arbitrary degree of accuracy. The only difficulty arises for the diagonal elements, which contain a singularity in the integrand. To evaluate the diagonal entries, the integral can be written [3]

$$\begin{aligned} \int_a^b H_0^{(2)}(kx) dx &= \int_a^b J_0(kx) dx - j \int_a^b \left[ Y_0(kx) - \frac{2}{\pi} \ln \left( \frac{\gamma kx}{2} \right) \right] dx \\ &\quad - j \frac{2}{\pi} \int_a^b \ln \left( \frac{\gamma kx}{2} \right) dx \end{aligned} \quad (2.18)$$

where we have separated the real and imaginary parts of the expression and added and subtracted an asymptotic form of the singular Neumann function  $Y_0$  for small arguments. Since the singularities in the second integrand cancel, the first two integrals can be computed by numerical quadrature. The final integral in Equation (2.18) contains a singularity but is easily evaluated analytically. A brief review of numerical quadrature is provided in Appendix A. As mentioned there, singular integrands can sometimes be treated using a quadrature rule that specifically incorporates the singularity. FORTRAN subroutines that compute Equation (2.8) by numerical quadrature are provided for illustration in Appendix C. As an alternative to quadrature, the series for the Hankel function in (2.12) may be integrated on a term-by-term basis.

To illustrate the accuracy of the single-point approximation employed in Equation (2.10), Table 2.1 presents numerical values for the off-diagonal matrix elements produced by a source cell with width equal to  $0.1\lambda_0$ , where  $\lambda_0$  is the free-space wavelength. (In all the examples discussed throughout this text, we will use units of free-space wavelength for the scatterer geometry. In these examples, the wavenumber  $k$  equals  $2\pi$ .) The “exact” results are obtained by numerical quadrature. For these data, the observation point is in the plane containing the source strip, thus maximizing the error in the single-point approximation. In this case, the error stabilizes at about 2% when the observer is more than  $0.2\lambda_0$  away from the center of the source cell. The error in the plane of the source cell remains at 2% even

**TABLE 2.1** Comparison of Exact and Single-Point Evaluation of Integral Used for Off-diagonal Matrix Entries

$x(\lambda_0)$	$\int_{-w_n/2}^{w_n/2} \frac{1}{4j} H_0^{(2)}(k x-x' ) dx'$		$\frac{w_n}{4j} H_0^{(2)}(kx)$		Percent Error
	Magnitude	Angle (deg)	Magnitude	Angle (deg)	
0.1	0.023662	-71.333	0.023605	-73.161	3
0.2	0.017147	-111.385	0.017348	-112.190	2
0.3	0.014131	-149.030	0.014334	-149.551	2
0.4	0.012289	174.063	0.012478	173.678	2
0.5	0.011017	137.490	0.011191	137.184	2
0.6	0.010071	101.095	0.010232	100.841	2
0.7	0.009331	64.807	0.009483	64.590	2
0.8	0.008734	28.588	0.008876	28.398	2
0.9	0.008238	-7.584	0.008373	-7.752	2

*Note:* The source cell has width equal to  $w_n = 0.1$ ;  $k = 2\pi$ .

in the far field. This error is primarily due to neglecting the partial interference that arises from the difference of up to  $0.1\lambda_0$  in path length across the source cell. Alternative ways of approximating Equation (2.8) can be developed that improve on the simple evaluation suggested above by building in the proper interference effects (Prob. P2.3).

An indication of the accuracy of the overall approach is illustrated by Tables 2.2 and 2.3. Values of the current density and scattering cross section found for different models of a circular cylinder illuminated by a TM plane wave are compared to the exact analytical solution. In each case, the models consist of  $N$  equal-sized cells with phase centers  $(x_n, y_n)$  located on the circular contour. Cell sizes were chosen so that the total circumference used in the model equals the original circumference of the cylinder ( $1\lambda_0$ ). Since we are using units of free-space wavelengths, the two-dimensional scattering cross section is also in wavelengths and is presented in decibels ( $\sigma_{\text{dB}} = 10 \log_{10} \sigma$ ). The matrix equation is

**TABLE 2.2** Current Density  $J_z$  Induced on Perfectly Conducting Cylinder Having  $1\lambda_0$  Circumference

$N$	Magnitude	Phase (deg)	Percent Error
a. For $\phi = \pi$			
8	0.006391	41.261	2.9
16	0.006302	41.134	1.7
32	0.006271	40.792	0.9
64	0.006254	40.567	0.4
128	0.006245	40.451	0.2
Exact	0.006237	40.335	
b. For $\phi = \pi/2$			
8	0.002983	-38.969	
16	0.003020	-39.651	
32	0.003009	-39.455	
64	0.003001	-39.304	
128	0.002997	-39.223	
Exact	0.002993	-39.140	
c. For $\phi = 0$			
8	0.000845	154.158	
16	0.000784	152.361	
32	0.000773	152.678	
64	0.000766	152.995	
128	0.000763	153.171	
Exact	0.000760	153.351	

*Note:* Comparison of numerical (EFIE) and exact results as a function of the number of basis functions. The wave is incident from the  $\phi = \pi$  direction.

**TABLE 2.3** Bistatic Scattering Cross Section  
 $\sigma_{TM}$  of Perfectly Conducting Cylinder Having  
 $1\lambda_0$  Circumference

$N$	$\phi = 0$	$\phi = \pi/2$	$\phi = \pi$
8	2.8339	-1.8739	-2.0299
16	2.8195	-1.8746	-2.0821
32	2.7947	-1.8783	-2.0959
64	2.7820	-1.8797	-2.1045
128	2.7755	-1.8805	-2.1087
Exact	2.7689	-1.8812	-2.1129

*Note:* In decibels free-space wavelength.  
 Comparison of numerical (EFIE) and exact  
 results for three observation angles as a  
 function of the number of basis functions.  
 The wave is incident from the  $\phi = \pi$  direction.

based on the approximate formulas of Equations (2.10) and (2.15). The numerical results appear to be converging to the exact solution as the model is refined, and it appears that accuracy of 1% in the current density is possible even in the shadow region of the cylinder, provided that the cell densities in use exceed  $32 \text{ cells}/\lambda_0$ . Because of the smooth nature of the scatterer, however, the circular cylinder example should be considered a “best case” unlikely to be representative of more complicated geometries.

As an additional illustration, Figure 2.3 compares two numerical solutions for the current density induced on one-half of a  $10\lambda_0 \times 3\lambda_0$  ogival cylinder. The 80-unknown

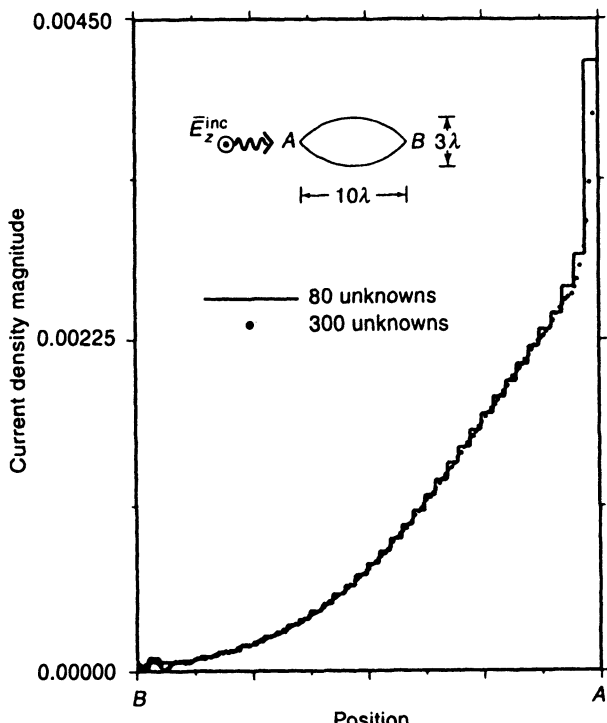


**Figure 2.3** The TM electric current density (EFIE result) induced on a  $10\lambda_0 \times 3\lambda_0$  ogival cylinder.

result employed cells with  $w_n \cong 0.265\lambda_0$ , larger than the recommended guideline of  $0.1\lambda_0$ . Despite the large cells, the current distribution obtained with 80 unknowns exhibits good agreement with the result obtained using 300 unknowns ( $w_n \cong 0.07\lambda_0$ ).

## 2.2 TE-WAVE SCATTERING FROM CONDUCTING CYLINDERS: MFIE DISCRETIZED WITH PULSE BASIS AND DELTA TESTING FUNCTIONS [1]

The scattering of TE fields incident upon an infinite, perfectly conducting cylinder (Figure 2.4) can also be analyzed using an integral equation formulation. The surface equivalence principle can be used to replace the perfectly conducting material by equivalent electric currents radiating in free space. For normally incident TE illumination, the field components present are  $H_z$ ,  $E_x$ , and  $E_y$ , and the equivalent current density has only a transverse component. Provided that the cylinder is a solid body and not a thin shell, an MFIE is convenient since only a single component of  $\bar{H}$  is present. If specialized to the TE polarization, the MFIE can be expressed as

$$H_z^{\text{inc}}(t) = -J_t(t) - \{\hat{z} \cdot \nabla \times \bar{A}\}_{S^+} = -J_t(t) - \left\{ \frac{\partial A_y}{\partial x} - \frac{\partial A_x}{\partial y} \right\}_{S^+} \quad (2.19)$$

where

$$\bar{A}(t) = \int \hat{t}(t') J_t(t') \frac{1}{4j} H_0^{(2)}(kR) dt' \quad (2.20)$$

and

$$R = \sqrt{[x(t) - x(t')]^2 + [y(t) - y(t')]^2} \quad (2.21)$$

In Equation (2.19), the subscript  $S^+$  is a reminder that the function in brackets is to be evaluated an infinitesimal distance outside the surface of the cylinder. The unit tangent vector along the surface can be expressed in terms of the orientation parameter  $\Omega$  defined in Figure 2.5 as

$$\hat{t}(t) = \hat{x} \cos \Omega(t) + \hat{y} \sin \Omega(t) \quad (2.22)$$

where  $t$  denotes the location around the contour.

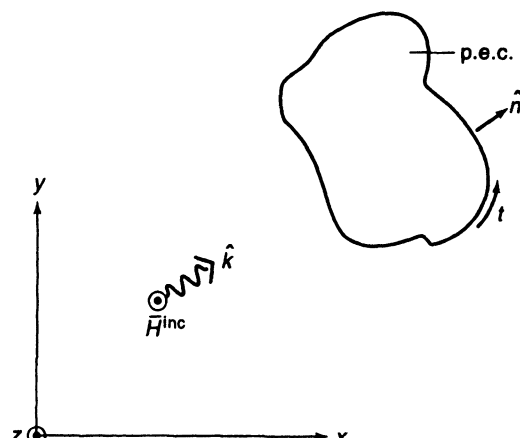


**Figure 2.4** A p.e.c. cylinder illuminated by an incident TE wave.

Following the procedure of Section 2.1, the cylinder contour is divided into  $N$  cells. The equivalent current density may be approximated by the superposition of subsectional pulse functions

$$p_n(t) = \begin{cases} 1 & \text{if } t \in \text{cell } n \\ 0 & \text{otherwise} \end{cases} \quad (2.23)$$

to produce

$$J_t(t) \cong \sum_{n=1}^N j_n p_n(t) \quad (2.24)$$

If (2.24) is substituted into (2.19), the resulting equation can be enforced at the centers of each of the  $N$  cells in the cylinder model (point matching) to produce the  $N \times N$  system

$$\begin{bmatrix} H_z^{\text{inc}}(t_1) \\ H_z^{\text{inc}}(t_2) \\ \vdots \\ H_z^{\text{inc}}(t_N) \end{bmatrix} = \begin{bmatrix} Z_{11} & Z_{12} & \cdots & Z_{1N} \\ Z_{21} & Z_{22} & & Z_{2N} \\ \vdots & \vdots & & \vdots \\ Z_{N1} & Z_{N2} & \cdots & Z_{NN} \end{bmatrix} \begin{bmatrix} j_1 \\ j_2 \\ \vdots \\ j_N \end{bmatrix} \quad (2.25)$$

The off-diagonal matrix elements are given by

$$Z_{mn} = \frac{k}{4j} \int_{\text{cell } n} \left( \sin \Omega(t') \frac{x_m - x(t')}{R_m} - \cos \Omega(t') \frac{y_m - y(t')}{R_m} \right) H_1^{(2)}(kR_m) dt' \quad (2.26)$$

where

$$R_m = \sqrt{[x_m - x(t')]^2 + [y_m - y(t')]^2} \quad (2.27)$$

The diagonal matrix entries can be obtained by constructing the limit

$$Z_{mm} = -1 + \lim_{x \rightarrow x_m, y \rightarrow y_m} \frac{k}{4j} \int_{\text{cell } m} \left( \sin \Omega(t') \frac{x - x(t')}{R} - \cos \Omega(t') \frac{y - y(t')}{R} \right) H_1^{(2)}(kR) dt' \quad (2.28)$$

as the observation point  $(x, y)$  approaches  $(x_m, y_m)$  from the exterior of  $S$ . The limiting procedure is easily carried out for flat cells (Prob. P2.8) and produces  $Z_{mm} = -\frac{1}{2}$  regardless of the cell size. In fact, the sole contribution to the integral arises from the immediate neighborhood of the singularity of the Green's function, since electric currents on a flat plane produce no tangential magnetic field elsewhere on the same plane. Therefore, even if the cells of the cylinder model are slightly curved, the diagonal matrix elements are approximately given by

$$Z_{mm} \cong -\frac{1}{2} \quad (2.29)$$

Although Equation (2.26) cannot be evaluated exactly, if the the cell sizes in the model are sufficiently small compared to the wavelength, a single-point evaluation similar to that employed for the TM example of Section 2.1 is possible and produces [1]

$$Z_{mn} \cong \frac{k w_n}{4j} \left( \sin \Omega_n \frac{x_m - x_n}{R_{mn}} - \cos \Omega_n \frac{y_m - y_n}{R_{mn}} \right) H_1^{(2)}(kR_{mn}) \quad (2.30)$$

where

$$R_{mn} = \sqrt{(x_m - x_n)^2 + (y_m - y_n)^2} \quad (2.31)$$

As will be shown below, Equation (2.30) can be a poor approximation to Equation (2.26) for closely spaced cells near corners. For better accuracy, it is a straightforward matter to evaluate Equation (2.26) over flat cells by numerical quadrature.

The simplest cylinder model consists of a flat-strip representation of the original contour, and the associated data structure incorporates the phase centers  $(x_n, y_n)$ , the widths  $w_n$ , and the orientation angles  $\Omega_n$  of each cell (Figure 2.5). This information allows an evaluation of the off-diagonal matrix entries using either the approximate formula (2.30) or a more exact numerical quadrature. Because the cell orientation is needed for the TE matrix entries, the modeling requirements are slightly more complicated than the TM EFIE example discussed in Section 2.1. (Since the TM currents flow in the  $\hat{z}$  direction, the cell orientation in the transverse plane is not critical as long as the cell is small with respect to the wavelength. For the TE polarization, the fields are maximized if the observer is in a direction perpendicular to the source cell; the fields are zero if the observer is in the plane of the cell. Thus, the cell orientation is a critical parameter.) It may be necessary to employ a large number of flat cells to represent a complex scatterer, and cylinder models that include the effect of cell curvature could be developed. Of course, a more sophisticated evaluation of (2.26) and (2.28) would be required in conjunction with better models.

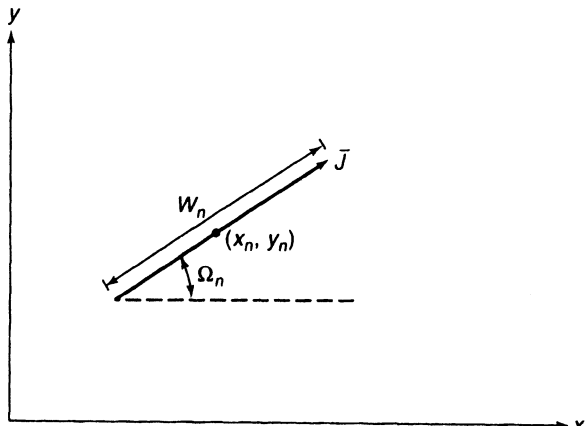


**Figure 2.5** Parameters describing a p.e.c. cell for the TE polarization.

Once Equation (2.25) is solved for the coefficients  $\{j_n\}$ , secondary quantities such as the bistatic scattering cross section may be computed. Details of the calculation are provided in Chapter 1. For the TE polarization, the bistatic scattering cross section can be approximated according to

$$\sigma_{TE}(\phi) \cong \frac{k}{4} \left| \sum_{n=1}^N j_n w_n \sin(\Omega_n - \phi) e^{jk(x_n \cos \phi + y_n \sin \phi)} \right|^2 \quad (2.32)$$

The overall accuracy of the approach is illustrated by Table 2.4, which compares the scattering cross section of a circular cylinder computed using the approximate formulas of Equations (2.29) and (2.30) with the exact solution for several different models employing equal-sized cells. In common with the EFIE formulation, the MFIE results are obtained using scatterer models that have the same circumference as the desired cylinder and phase

**TABLE 2.4** Two-dimensional Bistatic Scattering Cross Section as a Function of Observation Angle  $\phi$  and Number of Cells

$\phi$ (deg)	$N = 36$	$N = 72$	$N = 100$	Exact
0	10.93	10.82	10.79	10.70
30	3.68	3.86	3.90	4.00
60	1.82	2.01	2.06	2.17
90	0.92	0.72	0.68	0.53
120	3.23	2.97	2.91	2.74
150	3.96	4.04	4.06	4.09
180	3.31	3.40	3.43	3.47

*Note:* In decibels free-space wavelength. Numerical (MFIE) results are compared with the exact solution. The scatterer is a circular cylinder with circumference of  $5\lambda_0$ .

centers  $(x_n, y_n)$  located on the surface of the original cylinder. For the same  $5\lambda_0$  circular cylinder, Figure 2.6 shows the surface currents obtained from a discretization with  $N = 36$ . Despite the fact that the cell sizes are somewhat larger than the  $\lambda_0/10$  “rule of thumb,” the accuracy is good.

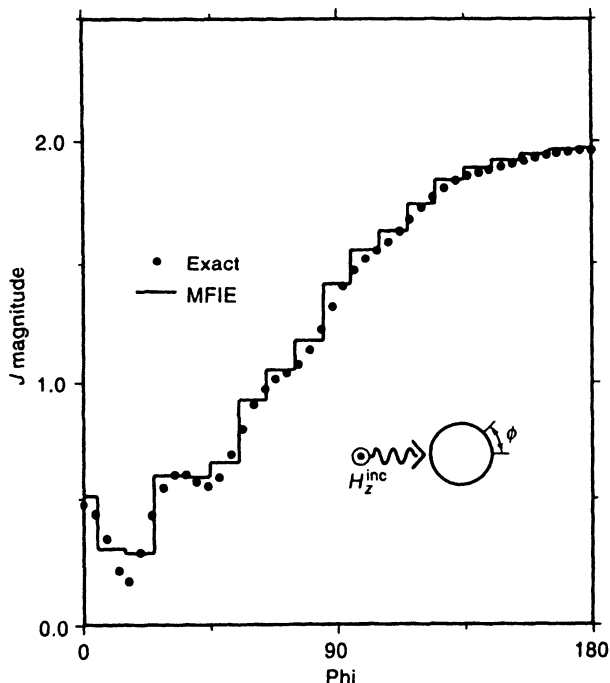


**Figure 2.6** Comparison of the numerical and exact results for the TE electric current density induced by a uniform plane wave on a p.e.c. circular cylinder with  $5\lambda$  circumference. The numerical (MFIE) result was obtained using 36 basis functions.

In order to judge the effect of the single-point approximation proposed in Equation (2.30), Table 2.5 compares numerical solutions for the surface current magnitude on a cylinder with circumference equal to  $1\lambda_0$ . These results were obtained using Equation (2.30), an accurate evaluation of (2.26) by quadrature, and the exact analytical solution. Clearly, the overall accuracy is improved by a more accurate evaluation of the matrix elements. In fact, Equation (2.30) is not a good approximation to (2.26) for closely spaced

**TABLE 2.5** Magnitude of Surface Current Density  $J_z$  Induced on a Circular, Perfectly Conducting Cylinder with Circumference  $1\lambda_0$  by an Incident TE Plane Wave Having Unity Magnitude  $H_z^{\text{inc}}$

$\phi$ (deg)	Equation (2.30)	Equation (2.26)	Exact
0	0.9742	0.9321	0.8882
36	0.7405	0.7267	0.7050
72	0.9363	0.9378	0.8914
108	1.517	1.478	1.410
144	1.778	1.708	1.656
180	1.829	1.749	1.707

*Note:* Results are reported as a function of observation angle  $\phi$  for a 10-cell model treated with the approximate formula (2.30) and an accurate evaluation of (2.26) by numerical quadrature. The exact analytical solution is also shown for comparison.

cells and is particularly poor in the vicinity of corners. To illustrate, Table 2.6 presents numerical data comparing scattered magnetic fields obtained using (2.30) and an accurate evaluation of (2.26) for an observer in the near zone of a source cell. Near the source, the error exceeds 8%. In fact, by comparing these data with Table 2.1, we conclude that the error in the single-point approximation is at least twice as bad for the scattered magnetic field calculation as it was for the scattered electric field calculation considered in Section 2.1. The additional error can be attributed to the presence of a differential operator in the source-field relationship for the TE case, which tends to amplify the error in the approximation. Because the magnetic field vanishes in the plane of the source strip, there is little interaction between adjacent cells for very smooth geometries, and the error will be minimal. However, the error is likely to be large for scatterers with corners.

**TABLE 2.6** Numerical Values of Scattered Magnetic Field

$x, y (\lambda_0)$	Using (2.26)		Using (2.30)		Percent Error
0.05	-0.1975	+j0.0240	-0.1807	+j0.0241	8.4
0.075	-0.1345	+j0.0349	-0.1279	+j0.0350	4.7
0.1	-0.1012	+j0.0445	-0.0982	+j0.0446	2.7
0.125	-0.0782	+j0.0524	-0.0766	+j0.0526	1.7
0.15	-0.0593	+j0.0583	-0.0584	+j0.0588	1.2
0.175	-0.0425	+j0.0625	-0.0418	+j0.0628	0.9
0.2	-0.0269	+j0.0643	-0.0264	+j0.0645	0.8
10.0	-0.00927	+j0.00104	-0.00934	+j0.00105	0.8

*Note:* As obtained from Equations (2.26) and (2.30) for an observer located along the line  $x = y$  with respect to a unit source located at the origin with  $w_n = 0.1$  and  $\Omega_n = 0$ . The wavenumber is  $k = 2\pi$ .

### 2.3. LIMITATIONS OF PULSE BASIS/DELTA TESTING DISCRETIZATIONS

The previous two examples used pulse basis functions and a procedure known as *point matching* to convert integral equations into matrix form. The discretizations appeared to produce stable, converging solutions as the number of expansion functions was increased. However, we sometimes encounter difficulties if we attempt to use a similar procedure to discretize the TE EFIE.

The source of the difficulty lies in the behavior of the fields produced by the pulse expansion functions. For the TE polarization, the  $\hat{x}$ -component of the electric field produced by an electric current density  $J_x$  can be found from a specialization of Equation (1.52) to obtain

$$E_x(x, y) = \frac{1}{j\omega\epsilon_0} \left( \frac{\partial^2}{\partial x^2} + k^2 \right) J_x * \frac{1}{4j} H_0^{(2)}(k\rho) \quad (2.33)$$

where the asterisk denotes two-dimensional convolution. An infinite strip of constant current density is depicted in Figure 2.7 and can be expressed mathematically as

$$J_x(x, y) = p(x; x_0, x_1)\delta(y) = \begin{cases} \delta(y) & x_0 < x < x_1 \\ 0 & \text{otherwise} \end{cases} \quad (2.34)$$

The source function can be obtained as

$$\left( \frac{\partial^2}{\partial x^2} + k^2 \right) J_x = [k^2 p(x; x_0, x_1) + \delta'(x - x_0) - \delta'(x - x_1)]\delta(y) \quad (2.35)$$

Therefore, the convolution of Equation (2.35) with the Green's function produces

$$\begin{aligned} E_x(x, y) &= \frac{-k^2}{4\omega\epsilon_0} \int_{x_0}^{x_1} H_0^{(2)}(kR) dx' \\ &\quad + \frac{1}{4\omega\epsilon_0} \left( \frac{\partial}{\partial x'} H_0^{(2)}(kR) \Big|_{x'=x_0} - \frac{\partial}{\partial x'} H_0^{(2)}(kR) \Big|_{x'=x_1} \right) \end{aligned} \quad (2.36)$$

where

$$R = \sqrt{(x - x')^2 + y^2} \quad (2.37)$$

Equation (2.36) reduces to

$$\begin{aligned} E_x(x, y) &= \frac{-k^2}{4\omega\epsilon_0} \int_{x_0}^{x_1} H_0^{(2)}(kR) dx' \\ &\quad - \frac{k}{4\omega\epsilon_0} \left( H_1^{(2)}(kR_0) \frac{x - x_0}{R_0} - H_1^{(2)}(kR_1) \frac{x - x_1}{R_1} \right) \end{aligned} \quad (2.38)$$

where

$$R_0 = \sqrt{(x - x_0)^2 + y^2} \quad (2.39)$$

$$R_1 = \sqrt{(x - x_1)^2 + y^2} \quad (2.40)$$

The terms  $R_0$  and  $R_1$  represent the distance from the observer to the leading and trailing edges of the current source.

The potential difficulty lies in the character of the Hankel function  $H_1(\alpha)$  for small arguments. The leading behavior for small  $\alpha$  is

$$H_1^{(2)}(\alpha) \approx \frac{j2}{\pi\alpha} \quad \text{as } \alpha \rightarrow 0 \quad (2.41)$$

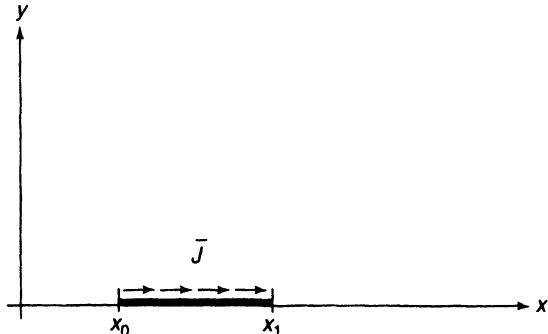


**Figure 2.7** Geometry of a source consisting of a transverse electric current density.

which indicates that the electric field produced by the constant pulse of current density  $J_x(x)$  is singular (infinite) at the edges of the source strip. The singular behavior can be related to the presence of line charges associated with the discontinuity in current density at the strip ends.

Now, consider the effect of using pulse basis functions to discretize the TE EFIE for a closed, perfectly conducting cylinder. For these basis functions, the moment method process requires that the cylinder geometry be represented by a finite number of cells over which the current density is assumed constant. Although we expect the true current density to be a continuous function along the cylinder perimeter, the discontinuous representation leads to the presence of fictitious line charges at the junctions between each cell in the model [4]. These line charges arise because the continuity equation (1.90) is implicitly built into the form of the EFIE operator used in Equation (2.33). These fictitious line charges give rise to infinite tangential electric fields at the cell junctions. If point matching is used to enforce the integral equation in the center of each cell, the matrix entries will be finite and a numerical solution can be found. However, because of the crude representation of the charge density, the accuracy is usually poor. Furthermore, as additional expansion functions are used in an attempt to get better results, the fictitious singularities at the cell edges may tend to dominate the near-zone scattered field and prevent the p.e.c. boundary condition  $\bar{E}_{\tan} = 0$  from being satisfied near the cell junctions. Although acceptable results can sometimes be obtained, there is no reason to expect numerical solutions produced by a pulse basis/point-matching discretization of the TE EFIE to improve as more and more expansion functions are employed.

The preceding example of Section 2.2 used pulse functions and point matching with the MFIE. Although the transverse electric field is singular at cell edges, the magnetic field  $H_z$  produced by a pulse basis function is finite along the source strip. Thus, the field singularities associated with the TE EFIE are not present in a TE MFIE formulation. As observed, the discretization of the MFIE appears to produce stable, converging solutions.

The example from Section 2.1 using the EFIE for TM-wave scattering also appeared to produce accurate solutions. In fact, the electric field produced by a  $\hat{z}$ -component of electric current density is finite and continuous throughout the source region. Because the fields and geometry are invariant with respect to  $z$ , the divergence of  $\bar{J}$  vanishes in the TM case. Thus, no fictitious line charges or field singularities are introduced from the use of pulse expansion functions with the EFIE for the TM polarization.

To discretize the EFIE for TE excitation and avoid the difficulties associated with fictitious line charges, we should employ smoother basis functions to eliminate the abrupt discontinuities in the current density. Subsectional triangle basis functions are illustrated in the following section. An alternate possibility is to generalize the point-matching procedure

used to enforce the integral equation. Instead of enforcing the equation at discrete points, it is possible to multiply both sides by a weighting or “testing” function and integrate over the cylinder surface. The equation is enforced in the sense of a weighted average, which can help compensate for discontinuities or singularities in the fields. To preserve the stability of the discretization,  $N$  linearly independent testing functions must be employed with  $N$  basis functions. The point-matching procedure is equivalent to the use of Dirac delta testing functions. The use of pulse testing functions will be described in the following section in the context of discretizing the TE EFIE.

In summary, there are a variety of cases where a pulse basis function/Dirac delta testing function discretization of an integral equation will produce accurate, converging numerical solutions. In other cases, however, the use of pulse functions introduces fictitious charge densities and undesired singularities in the fields. As a general rule, the proper choice of basis and testing functions must take into account the specific integro-differential operator to be discretized. This topic will be explored in Chapter 5. For the present discussion, it suffices to say that the basis and testing functions must contain enough smoothness to compensate for derivatives in the original equation. If we think of operators with weakly singular kernels (such as the TM EFIE) as the “baseline,” then the combination of pulse basis functions and Dirac delta testing functions provides the minimum degree of smoothness because the “baseline” operator can be discretized without the presence of singularities. However, pulse basis and point-matching discretizations are only well suited for use with equations that impose no additional derivatives within the operator. The TE EFIE involves two additional derivative operators, and thus two additional degrees of differentiability are required in the basis and testing functions in order to produce a robust discretization.

## **2.4 TE-WAVE SCATTERING FROM PERFECTLY CONDUCTING STRIPS OR CYLINDERS: EFIE DISCRETIZED WITH TRIANGLE BASIS AND PULSE TESTING FUNCTIONS [4]**

In Section 2.2, the MFIE was used to treat closed-body, perfectly conducting scatterers for the TE polarization. A disadvantage of the MFIE approach is that it cannot be used to treat infinitesimally thin structures (or any geometry with thickness much less than the wavelength) such as strips, plates, or scatterers with fins. The EFIE can be used for thin structures, but its implementation is slightly more complicated than the MFIE because of the differential operators appearing in the equation.

As discussed in the preceding section, it is advisable to use basis and testing functions having additional degrees of differentiability to compensate for the additional derivatives present in the TE EFIE. We will consider the use of subsectional triangle basis functions with pulse testing functions (Figure 2.8), which together provide two degrees of differentiability beyond that of the pulse/Dirac delta combination. For the TE polarization, the surface equivalence principle dictates that only a transverse component of equivalent surface current density  $\bar{J}$  is necessary to model the conducting material. Because we intend to use pulse testing functions, it will be particularly convenient to use the mixed-potential form of the EFIE, which for the TE case can be written as

$$\hat{\mathbf{t}} \cdot \bar{\mathbf{E}}^{\text{inc}} = jk\eta \hat{\mathbf{t}} \cdot \bar{\mathbf{A}} + \hat{\mathbf{t}} \cdot \nabla \Phi_e \quad (2.42)$$

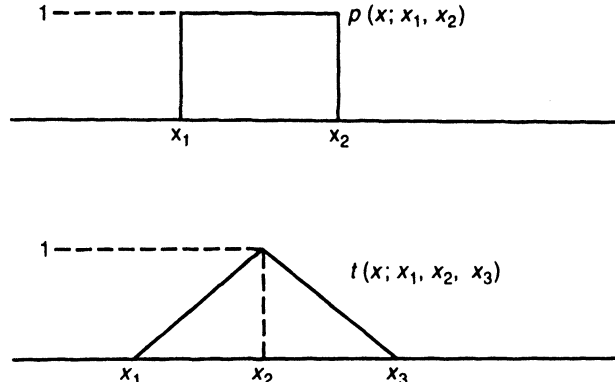


**Figure 2.8** Definition of pulse basis function  $p(x; x_1, x_2)$  and triangle basis function  $t(x; x_1, x_2, x_3)$ .

where  $\bar{A}$  is the magnetic vector potential

$$\bar{A}(t) = \int \hat{t}(t') J_t(t') \frac{1}{4j} H_0^{(2)}(kR) dt' \quad (2.43)$$

$\Phi_e$  is the electric scalar potential

$$\Phi_e(t) = \int \frac{\rho_e(t')}{\epsilon_o} \frac{1}{4j} H_0^{(2)}(kR) dt' \quad (2.44)$$

and, in practice, the continuity equation

$$-j\omega\rho_e = \nabla_s \cdot \bar{J} = \frac{\partial J_t}{\partial t} \quad (2.45)$$

is used to define the surface charge density  $\rho_e$ . As in the previous examples, Equation (2.42) is only valid for points on the surface of the original cylinder. In terms of the parametric variable  $t$  defined in Figure 2.4,

$$R = \sqrt{[x(t) - x(t')]^2 + [y(t) - y(t')]^2} \quad (2.46)$$

The contour of the cylinder can be modeled by the superposition of  $M$  flat strips, as depicted in Figure 2.9. Previous examples used pulse basis functions for the current density and assigned one basis function per strip in this type of model. In this example, we consider triangle basis functions that overlap two adjacent strips. The current density can be written in terms of the expansion functions and the coordinates shown in Figure 2.9 as

$$J_t(t) \cong \sum_{n=1}^N j_n t(t; t_{n-1}, t_n, t_{n+1}) \quad (2.47)$$

In the case of a closed cylinder, the basis functions overlap continuously around the contour, and there will be  $M$  basis functions for an  $M$ -cell model ( $N = M$ ). In the case of an open structure, the basis function adjacent to an edge is centered between the first and second strip pair and forces the current density to equal zero on the ends of the structure. This is consistent with the physical behavior that the current flowing into the strip edge must vanish. (Recall from Section 1.7 that the equivalent current density actually represents the superposition of the currents on both sides of the strip, and therefore  $J_t$  can not flow around the edge.) Thus, there will be  $M - 1$  basis functions for an open structure modeled with  $M$  cells ( $N = M - 1$ ).

A consequence of this type of basis function is that a minimum of 2 cells (strips) are required to model any structure, no matter how small that scatterer may be. In common

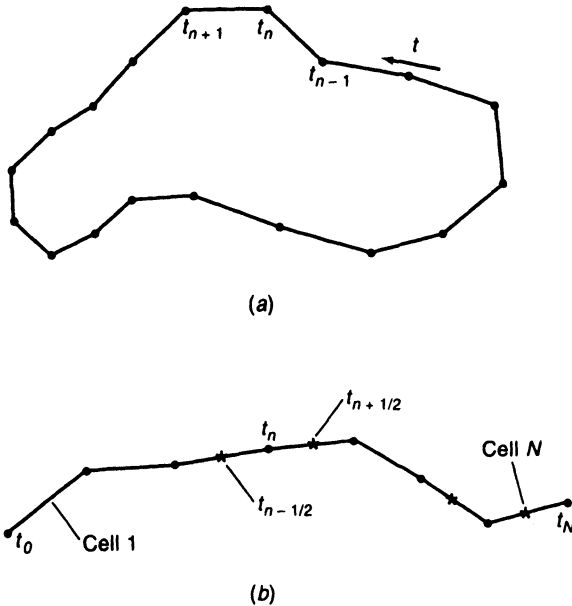


**Figure 2.9** (a) Flat-strip model of a closed-cylinder cross section. (b) Flat-strip model of the cross section of an open cylindrical structure.

with previous formulations, cell sizes must be much smaller than the wavelength in order to accurately represent the current density, and a minimum of 10 cells per wavelength is usually recommended.

The surface charge density consistent with a triangle basis function for  $J_t$  can be expressed as a combination of two pulse basis functions, each with support over one of the two original cells straddled by the subsectional triangle function. This combination of pulse functions is sometimes denoted a *pulse doublet*. The superposition of each doublet of charge density produces a pulse expansion, consistent with Equation (2.45), that can be written as

$$\frac{\rho_e(t)}{\epsilon_0} \cong \frac{-\eta}{jk} \sum_{n=1}^N j_n \left( \frac{1}{t_n - t_{n-1}} p(t; t_{n-1}, t_n) - \frac{1}{t_{n+1} - t_n} p(t; t_n, t_{n+1}) \right) \quad (2.48)$$

Equations (2.47) and (2.48) can be substituted into the vector and scalar potential functions, respectively.

The integral equation (2.42) can be enforced by “testing” the equation with pulse functions whose domain begins in the center of one strip and extends to the center of an adjacent strip. The process, a generalization of the point-matching approach employed in Sections 2.1 and 2.2 to approximately enforce the equation, involves multiplying both sides of the integral equation with a testing function and integrating over the scatterer surface (see Chapter 5 and [1]). For notational convenience, consider the numbering scheme proposed in Figure 2.9b. The testing function spanning strips  $m$  and  $m + 1$  is a pulse function defined as

$$T_m(t) = p(t; t_{m-1/2}, t_{m+1/2}) \quad (2.49)$$

The choice of pulse testing functions permits the analytical treatment of the gradient operator appearing in the mixed-potential form of the EFIE according to the idea

$$\int p(t; a, b) \hat{t}(t) \cdot \nabla F dt = \int_a^b \frac{dF}{dt} dt = F(b) - F(a) \quad (2.50)$$

Therefore, the pulse testing function absorbs the derivative present in the gradient operator.

After completing the discretization, the system of equations can be expressed as an  $N \times N$  matrix of the form

$$\begin{bmatrix} e_1 \\ e_2 \\ \vdots \\ e_N \end{bmatrix} = \begin{bmatrix} Z_{11} & Z_{12} & \cdots & Z_{1N} \\ Z_{21} & Z_{22} & & Z_{2N} \\ \vdots & \vdots & \ddots & \vdots \\ Z_{N1} & Z_{N2} & \cdots & Z_{NN} \end{bmatrix} \begin{bmatrix} j_1 \\ j_2 \\ \vdots \\ j_N \end{bmatrix} \quad (2.51)$$

where

$$e_m = \int_{t_{m-1/2}}^{t_{m+1/2}} \hat{i}(t) \cdot \bar{E}^{\text{inc}}(t) dt \quad (2.52)$$

$$\begin{aligned} Z_{mn} = & \frac{k\eta}{4} \int_{t_{m-1/2}}^{t_{m+1/2}} \hat{i}(t) \cdot \int_{t_{n-1}}^{t_{n+1}} \hat{i}(t') t(t'; t_{n-1}, t_n, t_{n+1}) H_0^{(2)}(kR) dt' dt \\ & + \frac{\eta}{4k} \left( \frac{1}{t_n - t_{n-1}} \int_{t_{n-1}}^{t_n} H_0^{(2)}(kR_2) dt' - \frac{1}{t_{n+1} - t_n} \int_{t_n}^{t_{n+1}} H_0^{(2)}(kR_2) dt' \right. \\ & \left. - \frac{1}{t_n - t_{n-1}} \int_{t_{n-1}}^{t_n} H_0^{(2)}(kR_1) dt' + \frac{1}{t_{n+1} - t_n} \int_{t_n}^{t_{n+1}} H_0^{(2)}(kR_1) dt' \right) \end{aligned} \quad (2.53)$$

$$R_1 = \sqrt{[x(t_{m-1/2}) - x(t')]^2 + [y(t_{m-1/2}) - y(t')]^2} \quad (2.54)$$

and

$$R_2 = \sqrt{[x(t_{m+1/2}) - x(t')]^2 + [y(t_{m+1/2}) - y(t')]^2} \quad (2.55)$$

The matrix entries of (2.53) can be evaluated to any necessary degree of accuracy by numerical quadrature. However, the two-dimensional quadrature required for the double integral may be time consuming, and it is worthwhile to consider a more efficient alternative. One possible approximation is given by

$$\begin{aligned} & \int_{t_{m-1/2}}^{t_{m+1/2}} \hat{i}(t) \cdot \int_{t_{n-1}}^{t_{n+1}} \hat{i}(t') t(t'; t_{n-1}, t_n, t_{n+1}) H_0^{(2)}(kR) dt' dt \\ & \cong [(t_m - t_{m-1/2})\hat{i}(t_{m-1/2}) + (t_{m+1/2} - t_m)\hat{i}(t_{m+1/2})] \\ & \cdot \left( \hat{i}(t_{n-1/2}) \int_{t_{n-1/2}}^{t_n} H_0^{(2)}(k\tilde{R}) dt' + \hat{i}(t_{n+1/2}) \int_{t_n}^{t_{n+1/2}} H_0^{(2)}(k\tilde{R}) dt' \right) \end{aligned} \quad (2.56)$$

where

$$\tilde{R} = \sqrt{[x(t_m) - x(t')]^2 + [y(t_m) - y(t')]^2} \quad (2.57)$$

This approximation reduces all the necessary integrals to the form

$$\int H_0^{(2)}(kR) dt' \quad (2.58)$$

where  $R$  is defined in Equation (2.46). Equation (2.58) is the same integral encountered in the TM EFIE example, and its evaluation has been discussed in Section 2.1.

There are several good reasons for considering the approximation introduced in Equation (2.56). The approximation is sensible and improves as the cell sizes are reduced. One

practical advantage of using the approximation is that it permits all of the integrals required for the matrix entry calculation to be evaluated by a common subroutine. An additional advantage is that it eliminates the need for time-consuming two-dimensional quadrature. In justification for the approximation, it is worth noting that as the cell sizes are made smaller and smaller compared to the wavelength, the matrix element  $Z_{mn}$  is dominated by the contribution from the scalar potential part (which is not affected by the approximation). For small cell sizes, the vector potential part is of secondary importance. (The decoupling of the scalar and vector potentials leads to numerical difficulties in the case of electrically small scatterers. These will be examined in the context of three-dimensional bodies in Chapter 10.)

The scattering cross section can be found once the coefficients  $\{j_n\}$  are obtained from the solution of Equation (2.51). An exact formula for the bistatic cross section that incorporates the flat-strip model and triangular basis functions is

$$\sigma_{TE}(\phi) = \frac{k}{4} \left| \sum_{n=1}^N \int_{t_{n-1}}^{t_{n+1}} [\hat{y} \cdot \hat{t}(t') \cos \phi - \hat{x} \cdot \hat{t}(t') \sin \phi] j_n \right. \\ \left. \times t(t'; t_{n-1}, t_n, t_{n+1}) e^{jk[x(t') \cos \phi + y(t') \sin \phi]} dt' \right|^2 \quad (2.59)$$

These integrals can either be evaluated in closed form or approximated for simplicity.

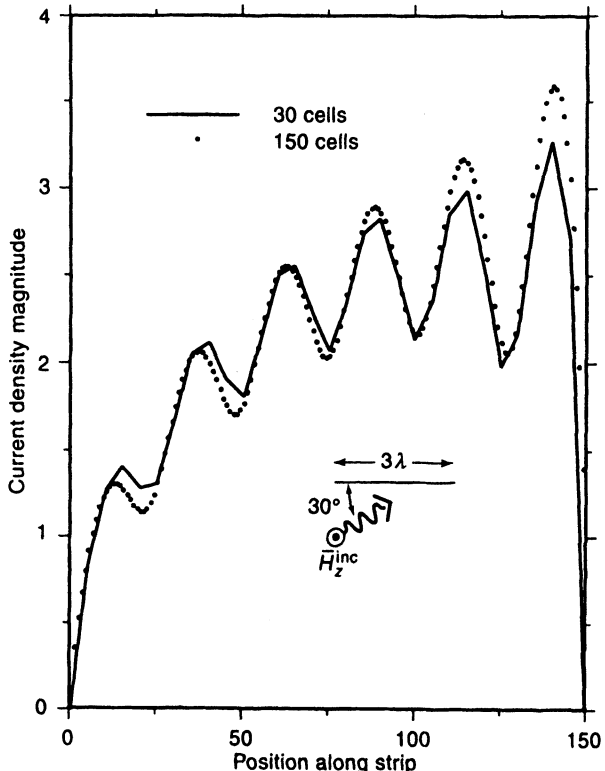
The accuracy of this moment method approach is illustrated by Table 2.7, which shows the scattering cross section of a circular cylinder produced by the above method compared to the exact eigenfunction solution. The numerical results appear to improve as the cell density is increased. As an illustration of a different geometry and one that cannot be treated using an MFIE, Figure 2.10 shows the current density induced on a flat strip of width  $3\lambda_0$ , obtained using a 10-cell/ $\lambda_0$  and a 50-cell/ $\lambda_0$  discretization.

TABLE 2.7 Bistatic Scattering Cross Section as a Function of Observation Angle  $\phi$  and Number of Cells

$\phi$ (deg)	$N = 10$	$N = 20$	$N = 40$	Exact
0	-6.83	-6.05	-5.88	-5.82
30	-8.78	-8.02	-7.84	-7.78
60	-10.94	-10.11	-9.90	-9.84
90	-6.72	-6.10	-5.95	-5.90
120	-3.94	-3.59	-3.51	-3.49
150	-2.90	-2.77	-2.75	-2.74
180	-2.67	-2.63	-2.64	-2.64

Note: In decibels free-space wavelength. The scatterer is a circular cylinder with circumference of  $1\lambda_0$  illuminated by a TE plane wave propagating in the  $\phi = 0$  direction. Triangle basis functions and pulse testing functions were used to discretize the EFIE.

It is worthwhile to investigate the relative accuracy of the MFIE formulation described in Section 2.2 and this EFIE approach. Table 2.8 compares the current density on a circular cylinder obtained using these two formulations. In addition, results are shown for an EFIE discretized with pulse basis functions and Dirac delta testing functions (the approach recommended *against* in Section 2.3) and an MFIE discretized with triangle basis functions and



**Figure 2.10** Two numerical (EFIE) results for the TE surface current density along a flat strip of  $3\lambda$  width. The first result is obtained with  $10 \text{ cells}/\lambda$ ; the second with  $50 \text{ cells}/\lambda$ .

Dirac delta functions (Prob. P2.11). The cylinder has  $1\lambda_0$  circumference and is represented with 40 equal-sized cells. By comparing these results with the exact analytical solution, it is apparent that the pulse/delta MFIE formulation and the triangle/pulse EFIE formulation exhibit similar accuracy and are substantially more accurate than the pulse/delta EFIE formulation. However, neither is as accurate for this problem as the triangle/delta MFIE approach suggested in Prob. P2.11.

A computer program to implement the TE EFIE approach described above will require a somewhat more complicated cylinder model than those employed in Sections 2.1 and 2.2. Because of the need for additional generality, including the possibility of junctions between multiple cells in the model, we consider the following scheme. First, we number the endpoints  $(x_n, y_n)$  of each strip used to represent the cylinder contour. (We often refer to the endpoints as *nodes* of the model.) Second, we number the cells themselves. Because of the manner in which the basis functions straddle two adjacent cells, it is convenient to construct a table linking the endpoints at which basis functions are centered to the adjacent cells. A second pointer array links each cell with the associated nodes. To illustrate this modeling scheme, Figure 2.11 shows a sample cylinder model and Table 2.9 contains the pointer arrays describing the *connectivity* between cells and nodes.

Scatterer models having junctions between strips or between strips and solid cylinders can also be treated using this EFIE formulation. Figure 2.11 depicts a hypothetical model containing several strip cells. Consider the cells numbered 4, 5, and 6, which form a junction at node 2. (Furthermore, suppose that these cells are located in open space rather than as a part of a closed scatterer.) It appears possible to represent the current flow through the junction of these three cells by superimposing three triangle basis functions (straddling cells 4 and 5, 5 and 6, and 4 and 6, respectively). However, only two of the basis functions

**TABLE 2.8** Comparison of Current Density Induced on a Circular Cylinder with Circumference  $1\lambda_0$  by TE Plane Wave Propagating in  $\phi = 0$  Direction

$\phi$ (deg)	EFIE		MFIE		
	Pulse/ Delta	Triangle/ Pulse	Pulse/ Delta	Triangle/ Delta	Exact
Magnitude					
0	0.8000	0.8875	0.8907	0.8891	0.8882
45	0.6386	0.6754	0.6733	0.6729	0.6722
90	1.1829	1.1741	1.1751	1.1708	1.1713
135	1.6052	1.6216	1.6232	1.6201	1.6199
180	1.6800	1.7084	1.7094	1.7076	1.7071
Phase (deg)					
0	68.69	66.89	66.29	66.66	66.56
45	119.06	113.83	113.41	113.57	113.56
90	-163.66	-164.88	-164.88	-164.80	-164.82
135	-125.65	-125.86	-125.83	-125.82	-125.84
180	-110.65	-110.85	-110.77	-110.82	-110.83

*Note:* An EFIE result obtained with pulse basis functions and Dirac delta testing functions is compared with the EFIE formulation of this section (triangle basis functions and pulse testing functions), the MFIE formulation of Section 2.2, another MFIE formulation (Prob. P2.11), and the exact solution. Each result was obtained using 40 equal-sized cells to represent the cylinder.

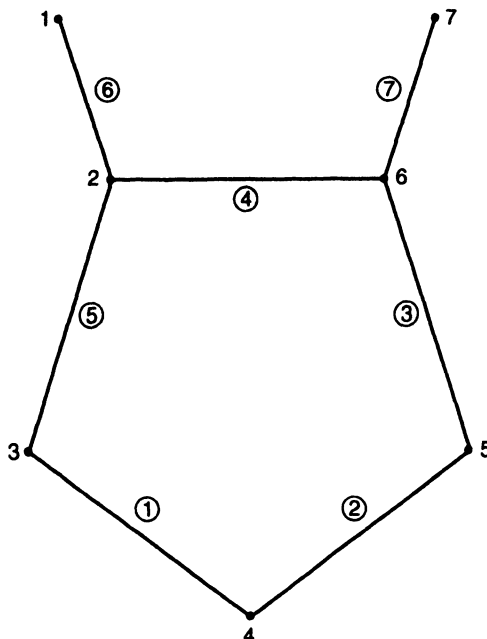


**Figure 2.11** Sample cylinder cross section depicting the indexing of nodes and cells used in the pointer arrays of Table 2.9.

are linearly independent. Therefore, it is necessary to arbitrarily discard one of the three functions, leaving two at the node  $(x_2, y_2)$ . If more than three cells join at a node, a similar procedure is followed using one fewer basis function than cells. With the exception of this adjustment, the numerical formulation proceeds as described above. Because of the way triangle basis functions straddle adjacent cells, Kirchhoff's current law is automatically satisfied at the junction.

**TABLE 2.9** Pointer Arrays Describing Cylinder Model in Figure 2.11

List of node locations	
$x_1$	$y_1$
$x_2$	$y_2$
•	•
•	•
•	•
$x_n$	$y_n$

Cell Index	Node 1	Node 2
Pointer from cell indices to node indices		
1	4	3
2	5	4
3	6	5
4	2	6
5	3	2
6	2	1
7	6	7

Node Index	Cell 1	Cell 2
Pointer from nodes where a basis function is located to adjacent cells		
2	5	6
2	5	4
6	4	7
6	4	3
5	3	2
4	2	1
3	1	5

## 2.5. TM-WAVE SCATTERING FROM INHOMOGENEOUS DIELECTRIC CYLINDERS: VOLUME EFIE DISCRETIZED WITH PULSE BASIS AND DELTA TESTING FUNCTIONS [5]

The preceding sections have examined surface integral equation formulations for scattering from conducting cylinders. An inhomogeneous dielectric cylinder characterized by a complex relative permittivity  $\epsilon_r(x, y)$  can be analyzed using a volume integral equation. The field components excited by a normally incident TM wave are  $E_z$ ,  $H_x$ , and  $H_y$ . Following

the volume equivalence principle discussed in Section 1.2, the dielectric material may be replaced by equivalent polarization currents

$$\bar{J}(x, y) = \hat{z} j \omega \epsilon_0 [\epsilon_r(x, y) - 1] E_z(x, y) \quad (2.60)$$

radiating in free space. For the TM polarization, the EFIE appearing in Equation (1.101) can be specialized to

$$E_z^{\text{inc}}(x, y) = \frac{J_z}{j \omega \epsilon_0 (\epsilon_r - 1)} + j \omega \mu_0 A_z \quad (2.61)$$

where

$$A_z(x, y) = \iint J_z(x', y') \frac{1}{4j} H_0^{(2)}(kR) dx' dy' \quad (2.62)$$

and

$$R = \sqrt{(x - x')^2 + (y - y')^2} \quad (2.63)$$

The specific form of Equation (2.61) is slightly different than Equation (1.101); here we have chosen  $J_z$  as the primary unknown instead of  $E_z$ .

The cylinder cross section can be divided into cells, as illustrated in Figure 2.12. If the unknown polarization current density is approximated by the superposition of subsectional pulse basis functions, defined in two-dimensional space as

$$p_n(x, y) = \begin{cases} 1 & \text{if } (x, y) \in \text{cell } n \\ 0 & \text{otherwise} \end{cases} \quad (2.64)$$

the current density can be expressed as

$$J_z(x, y) \cong \sum_{n=1}^N j_n p_n(x, y) \quad (2.65)$$

Equation (2.61) reduces to

$$E_z^{\text{inc}}(x, y) \cong \sum_{n=1}^N j_n \left( \frac{\eta p_n(x, y)}{jk[\epsilon_r(x, y) - 1]} + jk\eta \iint_{\text{cell } n} \frac{1}{4j} H_0^{(2)}(kR) dx' dy' \right) \quad (2.66)$$

Enforcing Equation (2.66) at the centers of each of the  $N$  cells produces an  $N \times N$  system

$$\begin{bmatrix} E_z^{\text{inc}}(x_1, y_1) \\ E_z^{\text{inc}}(x_2, y_2) \\ \vdots \\ E_z^{\text{inc}}(x_N, y_N) \end{bmatrix} = \begin{bmatrix} Z_{11} & Z_{12} & \cdots & Z_{1N} \\ Z_{21} & Z_{22} & & Z_{2N} \\ \vdots & \vdots & & \vdots \\ Z_{N1} & Z_{N2} & \cdots & Z_{NN} \end{bmatrix} \begin{bmatrix} j_1 \\ j_2 \\ \vdots \\ j_N \end{bmatrix} \quad (2.67)$$

whose entries are given by

$$Z_{mn} = \frac{k\eta}{4} \iint_{\text{cell } n} H_0^{(2)}(kR_m) dx' dy' \quad m \neq n \quad (2.68)$$

and

$$Z_{mm} = \frac{\eta}{jk(\epsilon_r m - 1)} + \frac{k\eta}{4} \iint_{\text{cell } m} H_0^{(2)}(kR_m) dx' dy' \quad (2.69)$$

where

$$R_m = \sqrt{(x_m - x')^2 + (y_m - y')^2} \quad (2.70)$$

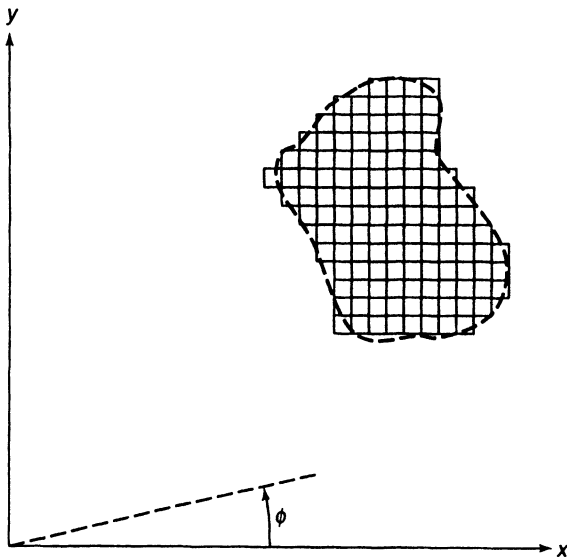


**Figure 2.12** Cross section of a dielectric cylinder illustrating the manner in which the region is divided into square cells.

In Equation (2.69),  $\varepsilon_{rn}$  is the average complex relative permittivity of the  $n$ th cell in the cylinder model.

Although the integrals in (2.68) and (2.69) must in general be evaluated by numerical quadrature, they can be evaluated analytically if the cell shapes are approximated by circles of the same area using [6, 6.684]

$$\int_{\phi'=0}^{2\pi} \int_{\rho'=0}^a H_0^{(2)}(kR)\rho' d\rho' d\phi' = \begin{cases} \frac{2\pi a}{k} J_0(k\rho)H_1^{(2)}(ka) - \frac{j4}{k^2} & \rho < a \\ \frac{2\pi a}{k} J_1(ka)H_0^{(2)}(k\rho) & \rho > a \end{cases} \quad (2.71)$$

where  $(\rho, \phi)$  represent conventional cylindrical coordinates,  $a$  denotes the radius of the equivalent circle,  $J_0$  and  $J_1$  are the Bessel functions of order zero and one, respectively, and  $H_1$  is the Hankel function of order one. Using the circular-cell approximation [5], we obtain

$$Z_{mn} = \frac{\eta\pi a_n}{2} J_1(ka_n)H_0^{(2)}(kR_{mn}) \quad m \neq n \quad (2.72)$$

where

$$R_{mn} = \sqrt{(x_m - x_n)^2 + (y_m - y_n)^2} \quad (2.73)$$

for the off-diagonal entries and

$$Z_{mm} = \frac{\eta\pi a_m}{2} H_1^{(2)}(ka_m) - \frac{j\eta\varepsilon_{rm}}{k(\varepsilon_{rm} - 1)} \quad (2.74)$$

for the diagonal entries. As a consequence of using  $J_z$  as the primary unknown instead of  $E_z$ ,  $\varepsilon_{rm}$  only appears in the diagonal matrix entries.

The solution of matrix equation (2.67) yields the coefficients  $\{j_n\}$ . Once the current density is obtained, other quantities such as the bistatic scattering cross section can be computed. Equation (1.137) can be specialized to this example to produce the scattering cross section

$$\sigma_{TM}(\phi) \cong \frac{k\eta^2}{4} \left| \sum_{n=1}^N j_n \frac{2\pi a_n}{k} J_1(ka_n) e^{jk(x_n \cos \phi + y_n \sin \phi)} \right|^2 \quad (2.75)$$

Assuming that we employ the approximate expressions based on Equation (2.71), the data structure used to store the cylinder model reduces to the phase center  $(x_n, y_n)$ , the equivalent radius  $a_n$ , and the average complex relative permittivity  $\varepsilon_{rn}$  for each cell in the model. Thus, the modeling is no more complicated than the approaches discussed in Sections 2.1 and 2.2.

Principal sources of error associated with the above procedure include the approximation of the polarization current by pulse basis functions (discretization error), the implicit assumption that  $\varepsilon_r(x, y)$  can be accurately modeled as a constant per cell, and the replacement of the original cylinder geometry by a superposition of cells that are approximately circular in shape (modeling errors). As in the previous examples of this chapter, each cell in the model must be relatively small in terms of the free-space wavelength. However, for this example the cells also must be small in terms of the wavelength in the dielectric medium. If  $\lambda_0$  is the free-space wavelength, we define the wavelength in the dielectric material as

$$\lambda_d = \frac{1}{\sqrt{|\varepsilon_r|}} \lambda_0 \quad (2.76)$$

In accordance with our usual “rule of thumb,” we recommend a minimum of 100 cells/ $\lambda_d^2$  of cross-sectional area.

Some indication of the accuracy of the overall moment method approach can be found by considering circular, homogeneous cylinders. Several models constructed with equal-sized square cells are shown in Figure 2.13. Tables 2.10 and 2.11 show the scattering cross section and internal  $E_z$ -field for a circular cylinder with circumference of  $0.5137\lambda_0$  and relative permittivity  $\varepsilon_r = 10$ . The numerical results are compared to the exact solutions. In these examples, the cross-sectional area of the models is scaled in order to equal that of the desired circular geometries. Figure 2.14 shows a comparison of internal  $E_z$ -fields for a cylinder with  $1.0\lambda_0$  circumference and relative permittivity  $\varepsilon_r = 2.56$ . Overall, the accuracy of the numerical result appears excellent.

**TABLE 2.10** Scattering Cross Section Obtained for Homogeneous Circular Dielectric Cylinder Having  $\varepsilon_r = 10$  and  $0.5137\lambda_0$  Circumference

$N$	$\sigma_{TM}$ (dB $\lambda_0$ )
21	-1.8484
61	-1.8469
101	-1.8442
Exact	-1.8426

*Note:* Comparison of numerical (EFIE) and exact results as a function of the number  $N$  of basis functions for  $\phi = \pi$ .

**TABLE 2.11** Electric Field  $E_z$  Induced at Center of Homogeneous Circular Dielectric Cylinder Having  $\varepsilon_r = 10$  and Circumference  $0.5137\lambda_0$  by Plane Wave with Unit Magnitude  $E_z^{inc}$

$N$	Magnitude	Phase
21	0.770	-94.75
61	0.779	-94.66
101	0.779	-94.75
Exact	0.780	-94.82

*Note:* Comparison of numerical (EFIE) and exact results as a function of the number  $N$  of basis functions.

Because exact results are available only for circular geometries having relatively simple permittivity profiles, it is desirable to have independent methods for estimating the accuracy of a given moment method solution. Since the boundary condition embodied in the integral equation is enforced only at the  $N$  match points, one way of studying the

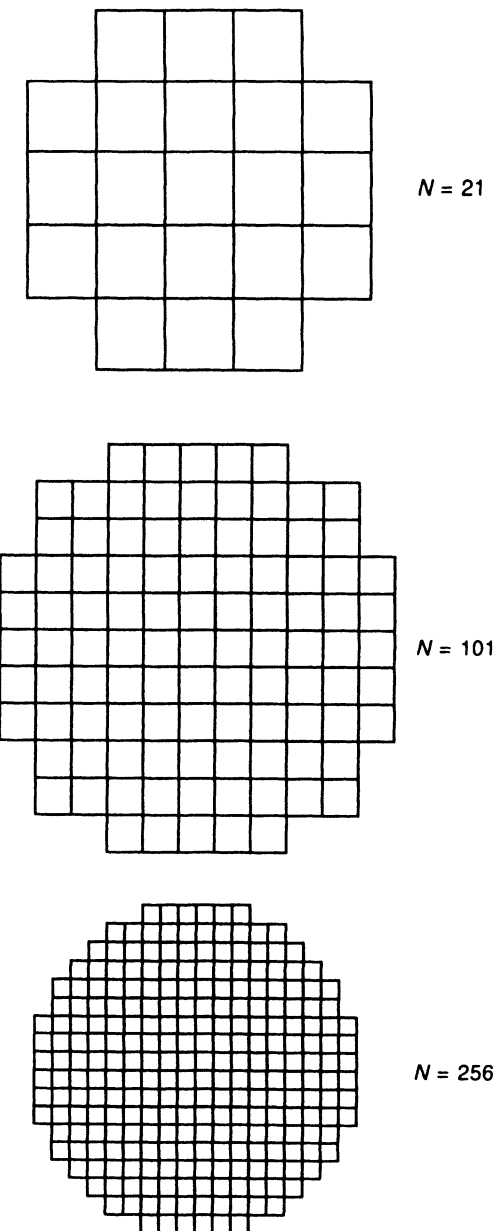
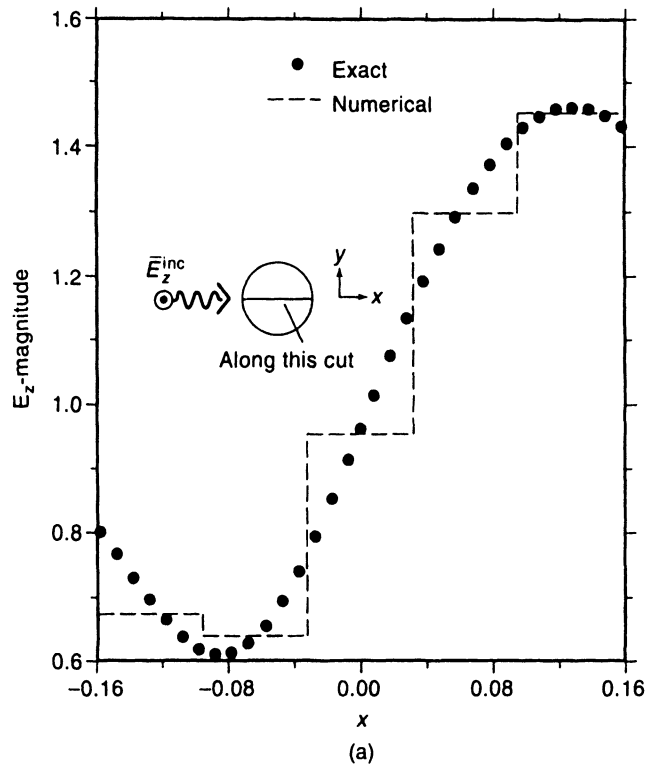


**Figure 2.13** Three models of circular dielectric cylinders.

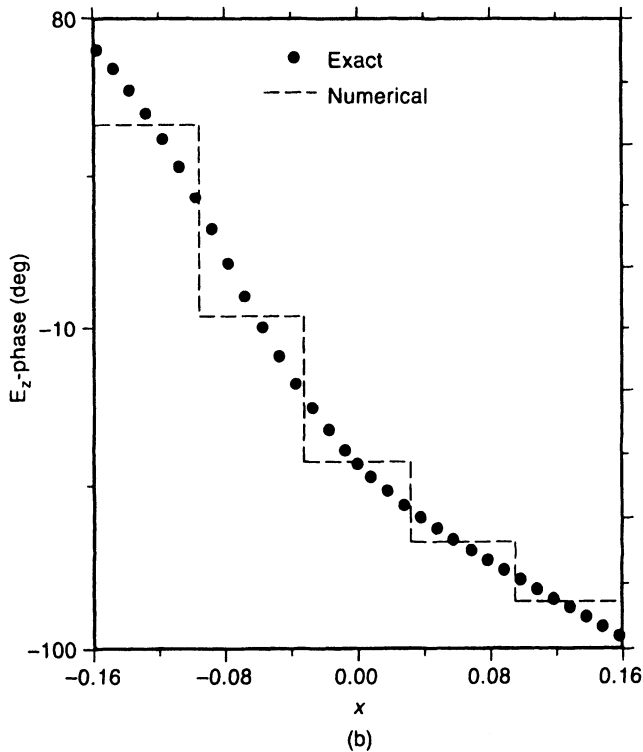
accuracy is to compute the electric field at other points within the cylinder. The boundary condition embodied in the relationship

$$E_z^{\text{inc}} = E_z - E_z^s \quad (2.77)$$

will be satisfied exactly only by the true solution, and thus we do not expect perfect agreement from our approximate result. The amount of deviation is indicative of the overall accuracy, however, and should provide useful guidance to aid an experienced user in estimating the accuracy of a given numerical result. Figure 2.15 shows the boundary condition error in magnitude for the example used in Figure 2.14.



(a)



(b)

**Figure 2.14** Comparison of the numerical and exact results for the TM electric field within a dielectric cylinder with circumference  $1.0\lambda_0$  and relative permittivity  $\epsilon_r = 2.56$ . The numerical results were obtained using 21 equal-sized cells (the first model in Figure 2.13) and the EFIE: (a) field magnitude; (b) field phase.

If greater accuracy for a given number of cells is desired, the above approach could be improved by incorporating a more flexible modeling scheme. In fact, it may be difficult to model highly heterogeneous permittivity profiles with “roughly circular” cells. Triangular or polygonal cells provide much greater flexibility at the cost of necessitating two-dimensional numerical integration to evaluate Equations (2.68) and (2.69) [7]. Additional accuracy could also be obtained by the use of smoother basis and testing functions.

Although we presented results for homogeneous cylinders to illustrate accuracy, the volume integral equation technique is intended for heterogeneous scatterers. For homogeneous geometries, the surface integral equation formulations described in Section 2.8 will usually be more computationally efficient alternatives.

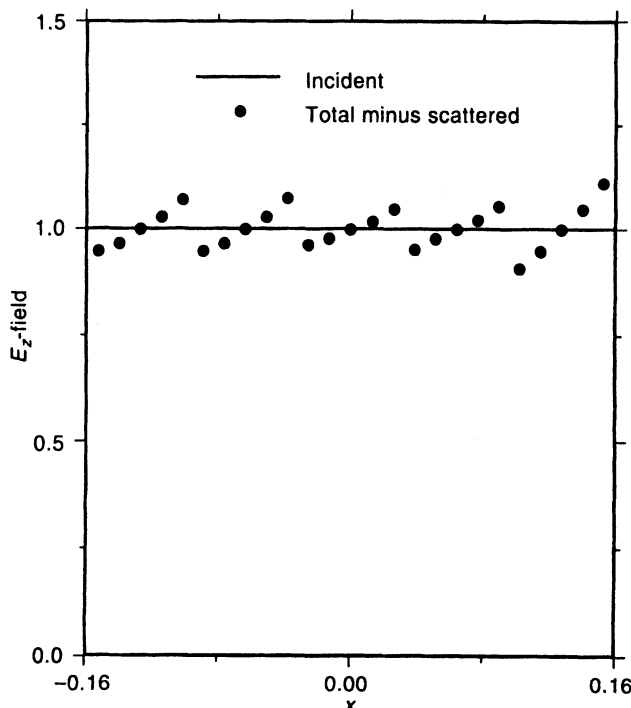


**Figure 2.15** Error in satisfying the electric field boundary condition for the TM example depicted in Figure 2.14.

## 2.6. TE-WAVE SCATTERING FROM DIELECTRIC CYLINDERS: VOLUME EFIE DISCRETIZED WITH PULSE BASIS AND DELTA TESTING FUNCTIONS [8]

An inhomogeneous dielectric cylinder illuminated by a normally incident TE wave can be treated in a manner analogous to that of the previous example, although we will see that the accuracy obtained with a similar pulse basis discretization can be significantly worse than that observed in the TM case. For the TE polarization, the field components present are  $H_z$ ,  $E_x$ , and  $E_y$ . The dielectric material may be replaced by equivalent electric polarization current densities

$$J_x(x, y) = j\omega\epsilon_0[\epsilon_r(x, y) - 1]E_x(x, y) \quad (2.78)$$

and

$$J_y(x, y) = j\omega\epsilon_0[\epsilon_r(x, y) - 1]E_y(x, y) \quad (2.79)$$

An electric field integral equation equivalent to (1.101) can be expressed in the form [8]

$$\bar{E}^{\text{inc}}(x, y) = \bar{E}(x, y) - \frac{\nabla \times (\nabla \times \bar{A}) - \bar{J}}{j\omega\epsilon_0} \quad (2.80)$$

Equation (2.80) can be separated into its components to produce the coupled system

$$E_x^{\text{inc}} = \frac{J_x\epsilon_r}{j\omega\epsilon_0(\epsilon_r - 1)} - \frac{1}{j\omega\epsilon_0} \left( \frac{\partial^2 A_y}{\partial x \partial y} - \frac{\partial^2 A_x}{\partial y^2} \right) \quad (2.81)$$

$$E_y^{\text{inc}} = \frac{J_y\epsilon_r}{j\omega\epsilon_0(\epsilon_r - 1)} - \frac{1}{j\omega\epsilon_0} \left( \frac{\partial^2 A_x}{\partial x \partial y} - \frac{\partial^2 A_y}{\partial x^2} \right) \quad (2.82)$$

where

$$\bar{A}(x, y) = \iint \bar{J}(x', y') \frac{1}{4j} H_0^{(2)}(kR) dx' dy' \quad (2.83)$$

and

$$R = \sqrt{(x - x')^2 + (y - y')^2} \quad (2.84)$$

If the cylinder cross section is divided into cells as depicted in Figure 2.12, and the current density is approximated by a superposition of pulse basis functions

$$\bar{J}(x, y) \cong \sum_{n=1}^N (\hat{x}j_{xn} + \hat{y}j_{yn}) p_n(x, y) \quad (2.85)$$

where

$$p_n(x, y) = \begin{cases} 1 & \text{if } (x, y) \in \text{cell } n \\ 0 & \text{otherwise} \end{cases} \quad (2.86)$$

Equations (2.81) and (2.82) can be enforced at the centers of each of the  $N$  cells to yield a  $2N \times 2N$  system of the form

$$\begin{bmatrix} E_x^{\text{inc}}(x_1, y_1) \\ E_x^{\text{inc}}(x_2, y_2) \\ \vdots \\ E_x^{\text{inc}}(x_N, y_N) \\ E_y^{\text{inc}}(x_1, y_1) \\ E_y^{\text{inc}}(x_2, y_2) \\ \vdots \\ E_y^{\text{inc}}(x_N, y_N) \end{bmatrix} = \begin{bmatrix} A_{11} & A_{12} & \cdots & A_{1N} & B_{11} & B_{12} & \cdots & B_{1N} \\ A_{21} & A_{22} & \cdots & A_{2N} & B_{21} & B_{22} & \cdots & B_{2N} \\ \vdots & \vdots & & \vdots & \vdots & \vdots & & \vdots \\ E_x^{\text{inc}}(x_1, y_1) & E_x^{\text{inc}}(x_2, y_2) & \cdots & E_x^{\text{inc}}(x_N, y_N) & E_y^{\text{inc}}(x_1, y_1) & E_y^{\text{inc}}(x_2, y_2) & \cdots & E_y^{\text{inc}}(x_N, y_N) \\ C_{11} & C_{12} & \cdots & C_{1N} & D_{11} & D_{12} & \cdots & D_{1N} \\ C_{21} & C_{22} & \cdots & C_{2N} & D_{21} & D_{22} & \cdots & D_{2N} \\ \vdots & \vdots & & \vdots & \vdots & \vdots & & \vdots \\ C_{N1} & C_{N2} & \cdots & C_{NN} & D_{N1} & D_{N2} & \cdots & D_{NN} \end{bmatrix} \begin{bmatrix} j_{x1} \\ j_{x2} \\ \vdots \\ j_{xN} \\ j_{y1} \\ j_{y2} \\ \vdots \\ j_{yN} \end{bmatrix} \quad (2.87)$$

Each of the four blocks of this system is an  $N \times N$  submatrix, with the specific entries given

in terms of the integral

$$I_n(x, y) = \iint_{\text{cell } n} H_0^{(2)}(kR) dx' dy' \quad (2.88)$$

as

$$A_{mn} = \frac{-\eta}{4k} \frac{\partial^2 I_n}{\partial y^2} \Big|_{x=x_m, y=y_m} \quad m \neq n \quad (2.89)$$

$$A_{mn} = \frac{\eta \varepsilon_{rm}}{jk(\varepsilon_{rm} - 1)} - \frac{\eta}{4k} \frac{\partial^2 I_m}{\partial y^2} \Big|_{x=x_m, y=y_m} \quad (2.90)$$

$$B_{mn} = C_{mn} = \frac{\eta}{4k} \frac{\partial^2 I_n}{\partial x \partial y} \Big|_{x=x_m, y=y_m} \quad (2.91)$$

$$D_{mn} = \frac{-\eta}{4k} \frac{\partial^2 I_n}{\partial x^2} \Big|_{x=x_m, y=y_m} \quad m \neq n \quad (2.92)$$

$$D_{mm} = \frac{\eta \varepsilon_{rm}}{jk(\varepsilon_{rm} - 1)} - \frac{\eta}{4k} \frac{\partial^2 I_m}{\partial x^2} \Big|_{x=x_m, y=y_m} \quad (2.93)$$

where  $\varepsilon_{rn}$  is the average complex-valued relative permittivity of cell  $n$ . If the cell shapes are approximated by circular cross sections, Equation (2.71) can be used to provide a closed-form evaluation of  $I_n$  and its derivatives [8]. We leave the detailed evaluation of the matrix entries as an exercise for the reader (Prob. P2.25).

If the circular-cell approximation suggested in the previous example (Section 2.5) is used for the TE case as well, the cylinder model necessary for computer implementation is limited to the phase centers  $(x_n, y_n)$ , the equivalent radii  $a_n$ , and the average relative permittivities of each cell. The cells in question must be small relative to the wavelength in the dielectric medium, as defined by Equation (2.76), and a reasonable minimum density is 100 cells/ $\lambda_d^2$ . Because there are two unknown coefficients per cell, this translates into 200 unknowns/ $\lambda_d^2$  of cross-sectional area.

After Equation (2.87) is solved for the coefficients  $\{j_{xn}\}$  and  $\{j_{yn}\}$  of the current distribution, secondary quantities such as the scattering cross section can be computed. Assuming a plane-wave incident field

$$H_z^{\text{inc}}(x, y) = e^{-jk(x \cos \phi^{\text{inc}} + y \sin \phi^{\text{inc}})} \quad (2.94)$$

the bistatic scattering cross section is given by

$$\sigma_{\text{TE}}(\phi) \cong \frac{k}{4} \left| \sum_{n=1}^N \frac{2\pi a_n}{k} J_1(ka_n) (j_{yn} \cos \phi - j_{xn} \sin \phi) e^{jk(x_n \cos \phi + y_n \sin \phi)} \right|^2 \quad (2.95)$$

The accuracy of the approach can be quite good for scatterers with permittivity not drastically different from that of the surrounding medium. Figure 2.16 shows the electric field within a circular, homogeneous cylinder having  $\varepsilon_r = 2.56 - j2.56$  and radius  $\lambda_0/\pi$ . These results were obtained using the square-cell model shown in Figure 2.13. The cross-sectional area of the model is scaled to equal that of the circular cylinder.

It was previously suggested that one way of estimating the error in an approximate solution is to check the degree to which the boundary condition embodied in the EFIE is satisfied. This has been carried out for an example illustrated in Figure 2.17. From a comparison with similar results presented for the TM polarization (Figure 2.15), we see a larger variation across each cell in the TE case. This might be expected due to the derivatives

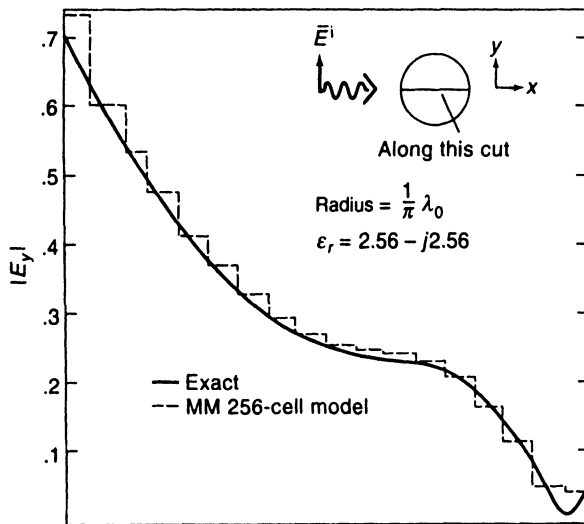


**Figure 2.16** Comparison of the numerical (EFIE) and exact results for the TE electric field magnitude within a dielectric cylinder with circumference  $2.0\lambda_0$  and relative permittivity  $\epsilon_r = 2.56 - j2.56$ . The numerical results were obtained using 256 equal-sized cells (the third model in Figure 2.13), equivalent to a cell density of 222 cells per square dielectric wavelength.

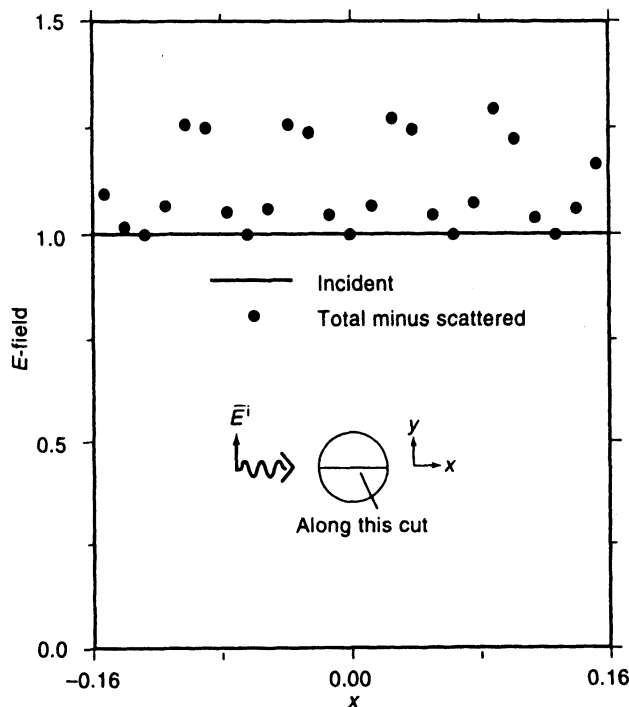


**Figure 2.17** Error in satisfying the electric field boundary condition for the TE polarization for a dielectric cylinder with circumference  $1.0\lambda_0$  and relative permittivity  $\epsilon_r = 2.56$ . The numerical (EFIE) results were obtained using the 21 equal-sized cell model depicted in Figure 2.13.

in the integral equation, which tend to amplify the error arising from approximations. Because of the additional derivatives in the TE EFIE, we expect to require smaller cell sizes to achieve the same accuracy as was possible for the TM example.

Unfortunately, smaller cell sizes are not enough to ensure accurate results, especially for larger values of  $\epsilon_r$ . For example, Figure 2.18 shows the magnitude and phase of the

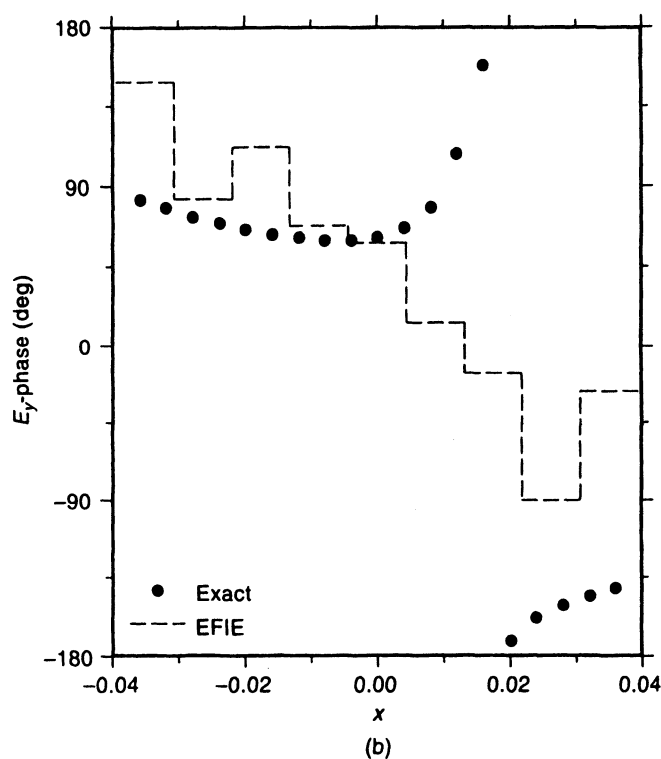
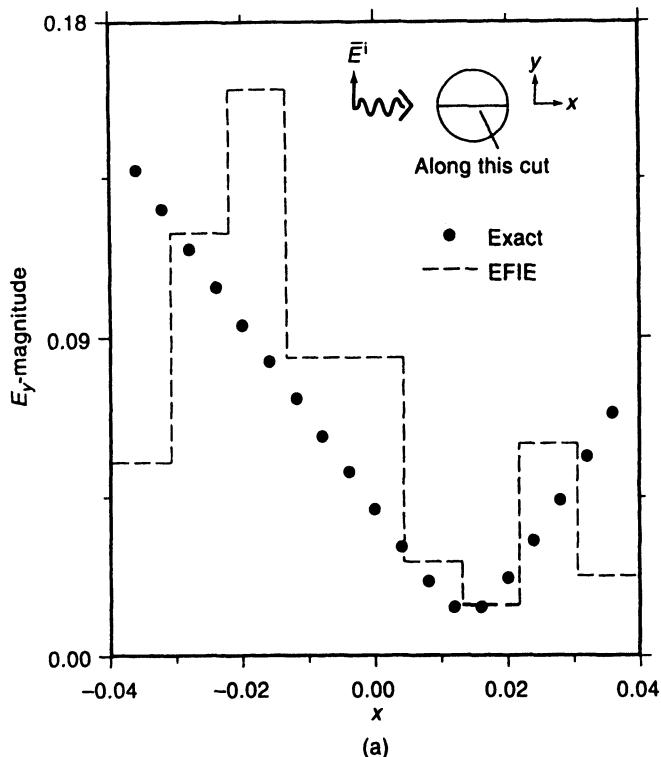


**Figure 2.18** Comparison of the numerical (EFIE) and exact results for the TE electric field within a dielectric cylinder with circumference  $0.248\lambda_0$  and relative permittivity  $\epsilon_r = 2 - j50$ . The numerical results were obtained using 61 equal-sized cells, for a density of 250 cells per square dielectric wavelength: (a) field magnitude; (b) field phase.

total electric field within a circular, homogeneous dielectric cylinder having  $\epsilon_r = 2 - j50$ . The cylinder has a circumference of  $0.248\lambda_0$ , and is modeled with 61 square cells. Clearly, the accuracy is poor, despite the fact that the cell density is  $250 \text{ cells}/\lambda_d^2$ . In addition, the results are very sensitive to changes in the cylinder model and get worse instead of better in this case as larger numbers of cells are used. A similar behavior is observed whenever the magnitude of  $\epsilon_r$  is greater than 10 and can probably be found for all values of  $\epsilon_r$ .

To understand the failure of the approach for large values of  $\epsilon_r$ , recall the previous discussion regarding the limitations associated with pulse basis functions and point matching for discretizing integro-differential equations. For the TE polarization, charge density is induced only at interfaces between homogeneous regions (or in regions with varying permittivity, which our model excludes from consideration). However, a fictitious surface charge density is introduced between each cell in the model through the pulse basis functions and the specific source–field relationship embodied in Equation (2.80). One effect of this charge is to produce fictitious discontinuities in the normal component of the electric field at each cell boundary. A second effect seems to be stronger fields in the vicinity of cell boundaries, as is apparent from Figure 2.17. As the cell sizes within the model decrease (as they must to maintain a fixed cell density relative to  $\lambda_d$  for increasing  $\epsilon_r$ ), the detrimental effects become more pronounced. In addition, the approximation employed to evaluate the matrix elements in closed form involved replacing the true cell shapes by circles, which changes the location of the fictitious charge layers. Hagmann and Levin have identified this approximation as a source of additional error [9]. Borup, Sullivan, and Gandhi have also investigated this formulation and report that significant errors are introduced due to the staircase approximation to the true cylinder surface necessitated by the square cell or circular cell modeling scheme [10]. Apparently, the local electric fields are a strong function of the precise location of surface charge density, and staircase boundaries are not adequate for placing the charge density in the proper location.

It is noteworthy that the TM approach presented in Section 2.5 (which involves no charge density since the divergence of the current density is zero) does not exhibit the instability or inaccuracy of the TE formulation. Better accuracy for the TE case might be obtained by employing smoother basis and testing functions in order to eliminate the fictitious charges. A triangular-cell discretization of the EFIE might also be in order to eliminate the staircase approximation of the true cylinder boundaries [7]. A third possibility is to use a volumetric MFIE formulation, which may prove less sensitive to proper charge modeling. The following section considers a combination of these three ideas.

## 2.7. TE-WAVE SCATTERING FROM INHOMOGENEOUS DIELECTRIC CYLINDERS: VOLUME MFIE DISCRETIZED WITH LINEAR PYRAMID BASIS AND DELTA TESTING FUNCTIONS [11]

The previous example employed the EFIE within a numerical formulation for TE-wave scattering from inhomogeneous dielectric cylinders. The MFIE can also be used to treat the TE problem and has several advantages over the specific EFIE approach discussed in the previous section.

For normally incident TE excitation, only a  $\hat{z}$ -component of the magnetic field is present. The dielectric material may be replaced by equivalent polarization currents ac-

cording to Equation (1.25), which in the two-dimensional situation specializes to

$$\bar{J}(x, y) = \frac{\epsilon_r(x, y) - 1}{\epsilon_r(x, y)} \nabla \times (\hat{z} H_z) = \frac{\epsilon_r(x, y) - 1}{\epsilon_r(x, y)} \left( \hat{x} \frac{\partial H_z}{\partial y} - \hat{y} \frac{\partial H_z}{\partial x} \right) \quad (2.96)$$

Using the source-field relationship presented in Equation (1.53), the MFIE may be expressed in the form

$$H_z^{\text{inc}}(x, y) = H_z(x, y) - \iint (\hat{z} \cdot \nabla' \times \bar{J}) \frac{1}{4j} H_0^{(2)}(kR) dx' dy' \quad (2.97)$$

where

$$R = \sqrt{(x - x')^2 + (y - y')^2} \quad (2.98)$$

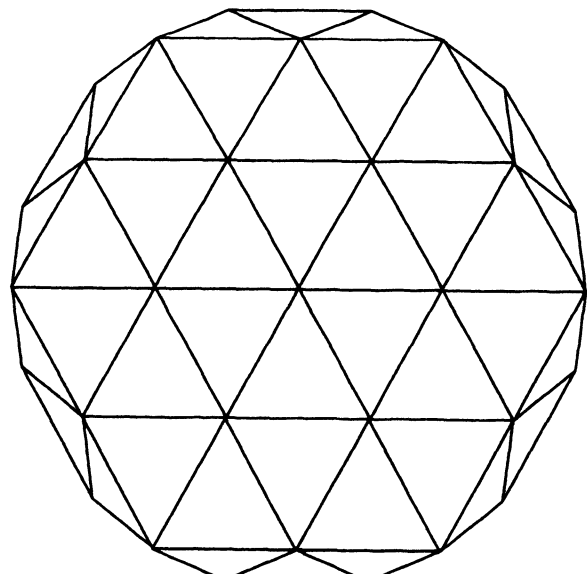
In general, the current density  $\bar{J}$  will exhibit an abrupt discontinuity at the cylinder edge. The domain of the integral appearing in Equation (2.97) must include the Dirac delta function arising from this discontinuity.

In a departure from the square-cell modeling scheme followed in the previous two sections, we consider a cylinder model comprised of triangular cells (Figure 2.19). Each cell in the model is assumed to have constant permittivity  $\epsilon_{rn}$ . Throughout the interior of the scatterer, the magnetic field is a continuous function and may be expanded in a basis consisting of a superposition of *linear pyramid functions* centered at each node of the triangular-cell model, so that

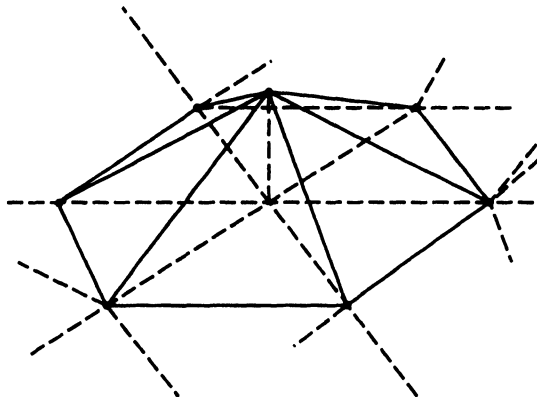
$$H_z(x, y) \cong \sum_{n=1}^N h_n P_n(x, y) \quad (2.99)$$

Figure 2.20 illustrates this type of expansion function. Each basis function straddles the triangular cells grouped around a given vertex and vanishes at every other node in the model. The expansion in (2.99) is a piecewise-linear interpolation between each node of the model, and the coefficient  $h_n$  represents the value of  $H_z$  at  $(x_n, y_n)$ . Within a cell,

$$H_z(x, y) = c_1 + c_2 x + c_3 y \quad (2.100)$$



**Figure 2.19** Triangular-cell model representing the cross section of a circular cylinder. The model involves 31 nodes, 42 cells, and 72 edges.



**Figure 2.20** Linear pyramid basis function. The function has unit value at one node of a triangular-cell model and is zero at all other nodes.

where  $c_1$ ,  $c_2$ , and  $c_3$  are constants that can be easily determined from the values of  $H_z$  at the cell corners (Prob. P2.26). It follows from Equation (2.96) that the current density will be constant within each cell. In terms of the coefficients  $\{h_n\}$  of the three basis functions overlapping a particular cell, the current density is given by

$$J_x = \frac{\varepsilon_{rn} - 1}{\varepsilon_{rn}} \frac{h_1(x_3 - x_2) + h_2(x_1 - x_3) + h_3(x_2 - x_1)}{y_1(x_3 - x_2) + y_2(x_1 - x_3) + y_3(x_2 - x_1)} \quad (2.101)$$

and

$$J_y = \frac{\varepsilon_{rn} - 1}{\varepsilon_{rn}} \frac{h_1(y_3 - y_2) + h_2(y_1 - y_3) + h_3(y_2 - y_1)}{x_1(x_3 - x_2) + x_2(x_1 - x_3) + x_3(x_2 - x_1)} \quad (2.102)$$

where  $h_n$  is the magnetic field at corner  $(x_n, y_n)$ . Since the scattered magnetic field produced by these equivalent sources is a continuous function across cell boundaries, it suffices to point match the MFIE at the nodes of the model. This provides one equation for each basis function, which can be arranged in matrix form as

$$\begin{bmatrix} H_z^{\text{inc}}(x_1, y_1) \\ H_z^{\text{inc}}(x_2, y_2) \\ \vdots \\ H_z^{\text{inc}}(x_N, y_N) \end{bmatrix} = \begin{bmatrix} Z_{11} & Z_{12} & \cdots & Z_{1N} \\ Z_{21} & Z_{22} & \cdots & Z_{2N} \\ \vdots & \vdots & \ddots & \vdots \\ Z_{N1} & \cdots & \cdots & Z_{NN} \end{bmatrix} \begin{bmatrix} h_1 \\ h_2 \\ \vdots \\ h_N \end{bmatrix} \quad (2.103)$$

As a consequence of the piecewise-constant representation employed for the current density, the curl operator appearing in Equation (2.97) produces a Dirac delta function over each cell edge. In other words, the two-dimensional integration required in (2.97) collapses to a one-dimensional integral over each cell edge in the model. An explicit expression for  $Z_{mn}$  in terms of the coefficients  $\{h_n\}$  is rather complicated and not needed to implement the scheme. It is more convenient to consider each edge of the model as a source and obtain an expression for the contribution from that edge to the entries of (2.103).

Figure 2.21 depicts a hypothetical edge located between cells 1 and 2 and a local coordinate system  $(n, t)$  associated with the normal and tangential directions. At this edge, the source function can be written

$$\hat{z} \cdot \nabla \times \bar{J} = \frac{\partial J_t}{\partial n} = (J_{t2} - J_{t1}) \delta(n) \quad (2.104)$$

where  $\delta(n)$  denotes a Dirac delta function having support at the edge and  $J_{ti}$  is the component

of equivalent current density in cell  $i$  tangential to the edge. Equations (2.101) and (2.102) provide the functional dependence of the current density on the coefficients  $\{h_n\}$ , the node locations  $\{x_n, y_n\}$ , and the cell permittivity  $\epsilon_{rn}$ . For a particular edge, these equations can be combined to determine the four weighting factors associated with the coefficients. We leave this calculation as an exercise (Prob. P2.27). The contribution from a given edge in the model to row  $m$  of the  $N \times N$  matrix of Equation (2.103) can be expressed as

$$(\alpha_1 h_1 + \alpha_2 h_2 + \alpha_3 h_3 + \alpha_4 h_4) \int \frac{1}{4j} H_0^{(2)}(kR) dt' \quad (2.105)$$

where  $\{\alpha_n\}$  are the weighting coefficients and  $R$  is the distance from the source point on the edge to node  $(x_m, y_m)$ . The equivalent source at each edge contributes to four locations in each row of the matrix (three locations if the edge is located on the outer surface of the cylinder). The evaluation of the integral over the Hankel function has been discussed in Section 2.1.

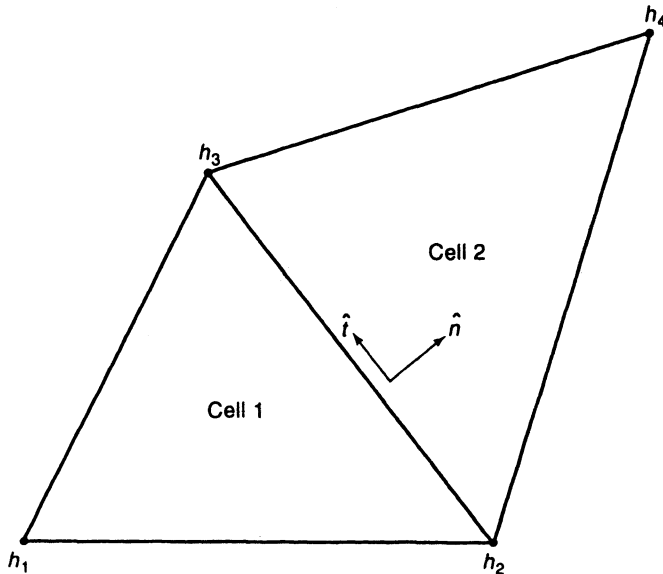


**Figure 2.21** Local geometry of a source edge between two triangular cells, with the indices associated with the magnetic field indicated at the nodes.

The complete matrix can be constructed by systematically scanning through each edge in the model and computing the contribution of Equation (2.104) to each row of the matrix. Once the coefficients  $\{h_n\}$  are determined from the solution of the matrix equation, the interior electric fields can be found from (2.101), (2.102), and

$$\bar{E} = \frac{-j\eta}{k(\epsilon_r - 1)} \bar{J} \quad (2.106)$$

Assuming that the incident magnetic field has unity magnitude, the bistatic scattering cross section is given by

$$\sigma_{TE}(\phi) = \frac{1}{4k} \left| \iint (\hat{z} \cdot \nabla' \times \bar{J}) e^{jk(x' \cos \phi + y' \sin \phi)} dx' dy' \right|^2 \quad (2.107)$$

The integration in (2.107) collapses to the cell edges and can be approximated by a summation for convenience.

To illustrate the accuracy of this procedure, Figure 2.22 shows a plot of the internal  $H_z$ -field within a circular, homogeneous cylinder having circumference of  $1\lambda_0$  and  $\epsilon_r = 2.56$ . Several different triangular-cell models were employed, with each scaled to have the same cross-sectional area as the desired circular cylinder. The numerical results appear to be converging toward the exact solution.

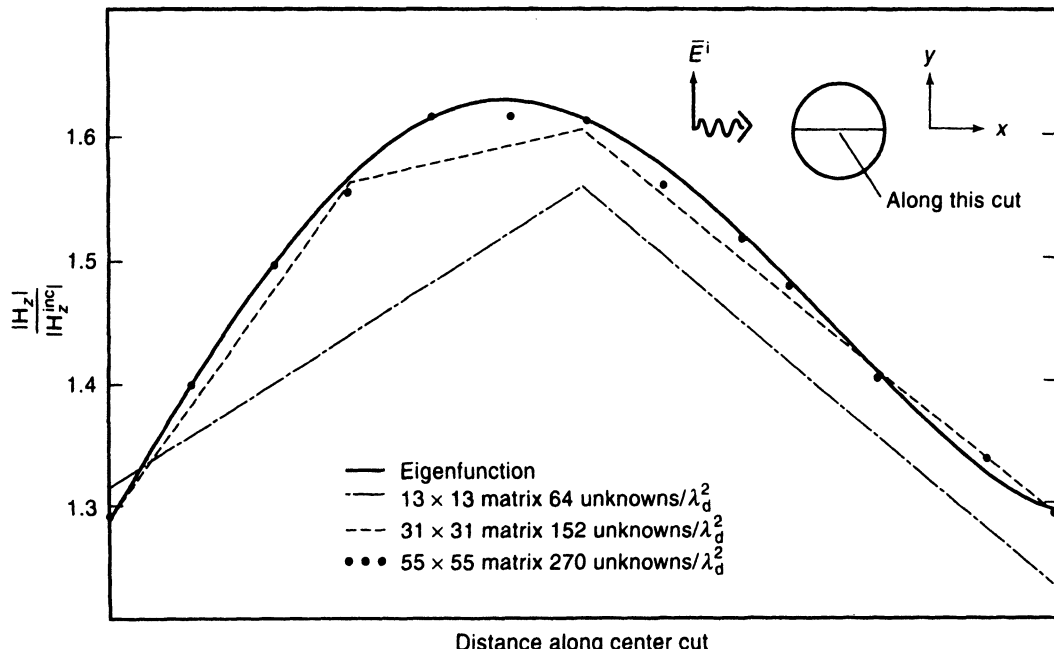


**Figure 2.22** The TE magnetic field within a circular, homogeneous dielectric cylinder with circumference  $1.0\lambda_0$  and relative permittivity  $\epsilon_r = 2.56$  (exact and MFIE results). After [11]. ©1988 IEEE.

It is often desired to compute the electric field within dielectric materials, and Equation (2.106) can be employed to generate the electric field as a secondary calculation once the numerical solution for  $H_z$  is obtained. Figure 2.23 shows the electric field within a layered dielectric cylinder having outer radius  $0.15\lambda_0$ , core relative permittivity  $\epsilon_r = 10 - j5$ , and cladding relative permittivity  $\epsilon_r = 6$ . The numerical result was obtained using a cylinder model with 196 triangular cells and 115 nodes. Agreement between the numerical result and the exact solution is excellent.

To provide a comparison between this formulation and the TE EFIE approach of the previous section, Table 2.12 shows the scattering cross section produced by both approaches for a circular cylinder with  $\epsilon_r = 2.56 - j2.56$  and circumference  $2.0\lambda_0$ . The results are presented as a function of the required number of unknowns. For this case and for a variety of other examples [11], the MFIE result is more accurate for a given number of unknowns than the pulse basis/delta testing EFIE result. Much of the improvement in accuracy can likely be attributed to the triangular-cell model employed with the MFIE formulation, which allows a much better approximation of the circular cross section than the square-cell model used with the EFIE.

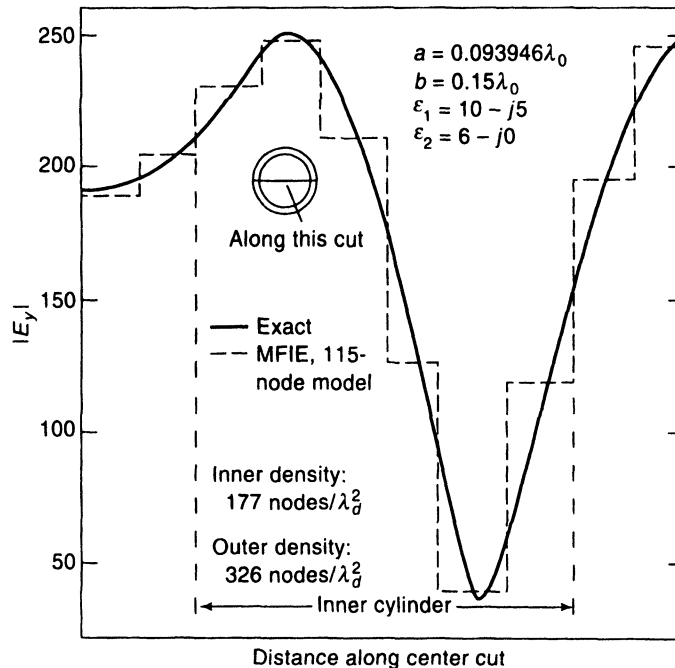


**Figure 2.23** The TE electric field within a layered dielectric cylinder (exact and MFIE results). After [11]. ©1998 IEEE.

**TABLE 2.12** Comparison of TE Bistatic Scattering Cross Section<sup>a</sup> for Dielectric Cylinder with  $\epsilon_r = 2.56 - j2.56$  and Circumference  $2.0\lambda_0$

$\phi$ (deg)	EFIE		MFIE		
	42 Unknowns	512 Unknowns	31 Unknowns	55 Unknowns	Exact
0	6.19	5.76	5.54	5.57	5.58
30	3.02	2.51	2.53	2.45	2.36
60	-6.79	-6.24	-5.54	-5.74	-5.94
90	-7.76	-7.91	-7.32	-7.66	-7.94
120	-14.19	-15.01	-13.08	-14.26	-15.12
150	-9.79	-9.48	-8.84	-8.89	-8.85
180	-6.98	-7.20	-6.15	-6.35	-6.45

<sup>a</sup> In decibels free-space wavelength.

*Note:* Numerical results obtained from the EFIE of Section 2.6 (square-cell models) are compared to results from the MFIE of Section 2.7 (triangular-cell models) and the exact solution. The matrix order is provided with each result.

The instabilities mentioned in connection with the TE EFIE do not seem to arise with the MFIE approach. As an example, Figure 2.24 shows the internal electric field produced by the MFIE formulation for the lossy dielectric cylinder of radius  $0.248\lambda_0$  and  $\epsilon_r = 2 - j50$ . Clearly, the MFIE result is superior to the EFIE result shown in Figure 2.18. The additional accuracy obtained from the MFIE formulation appears to be the result of several factors. The particular scheme employed to discretize the MFIE in this section employs a continuous

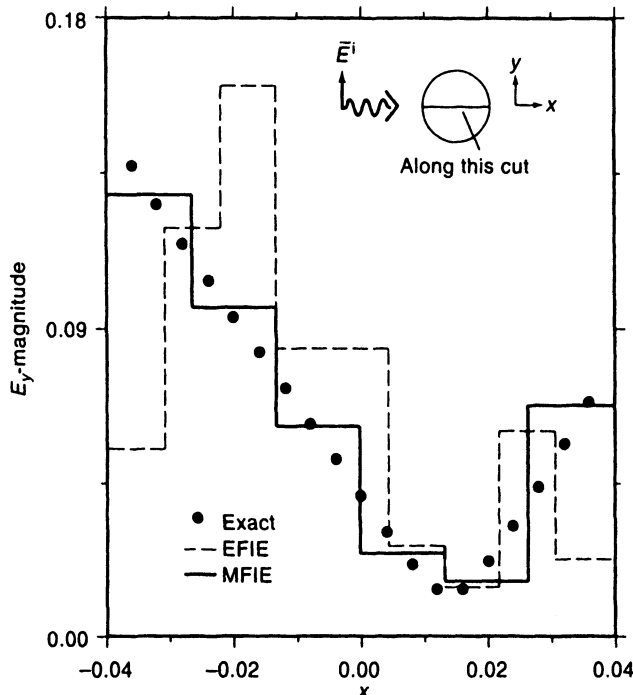


**Figure 2.24** The TE electric field produced by the volume MFIE for the identical scattering problem presented in Figure 2.18. The MFIE result used an 84-cell model resulting in a matrix of order 55.

representation for the primary unknown ( $H_z$ ) and in the process eliminates fictitious charge densities (Prob. P2.26). In addition, more accurate modeling is possible because of the flexibility associated with triangular cells. Finally, the TE MFIE operator itself seems to be more stable for numerical discretization than the TE EFIE operator.

The price to be paid for the flexibility of triangular cells is the additional complexity associated with the cylinder model. The cylinder model used with this MFIE formulation consists of a list of nodes  $\{x_n, y_n\}$ , a list of the relative permittivities of each cell, an array to act as a pointer from the cell indices to the three associated node indices, a second array to act as a pointer from the edge indices to the adjacent cell indices, and for convenience a third pointer array to link edge indices with the nodes defining the edge. This model exhibits a significant increase in complexity as compared with the simple models required with the EFIE approaches of Sections 2.5 and 2.6.

## 2.8. SCATTERING FROM HOMOGENEOUS DIELECTRIC CYLINDERS: SURFACE INTEGRAL EQUATIONS DISCRETIZED WITH PULSE BASIS AND DELTA TESTING FUNCTIONS [12]

A volume discretization is necessary to properly model a heterogeneous scatterer. However, homogeneous or layered geometries can be treated with surface integral equation formulations. Since the basis and testing functions are confined to the surfaces, rather than

distributed throughout the volume of the scatterer, far fewer unknowns arise with surface integral equations as the electrical size of the scatterer increases. Therefore, they are usually considered a much more efficient alternative than the volume equations discussed previously, provided the geometry in question consists of relatively few homogeneous regions.

A homogeneous cylinder characterized by permittivity  $\epsilon_d$  and permeability  $\mu_d$  is depicted in Figure 2.25. Suppose this cylinder is illuminated by a TM wave. According to the surface equivalence principle, equivalent sources  $J_z$  and  $K_t$  defined on the cylinder surface  $S$  are sufficient to represent either the exterior or interior problem. Coupled EFIEs were developed in Section 1.9 and can be specialized to the TM polarization to produce

$$E_z^{\text{inc}}(t) = K_t(t) + jk_0\eta_0 A_z^{(0)} + \left\{ \frac{\partial F_y^{(0)}}{\partial x} - \frac{\partial F_x^{(0)}}{\partial y} \right\}_{S^+} \quad (2.108)$$

$$0 = -K_t(t) + jk_d\eta_d A_z^{(d)} + \left\{ \frac{\partial F_y^{(d)}}{\partial x} - \frac{\partial F_x^{(d)}}{\partial y} \right\}_{S^-} \quad (2.109)$$

where  $t$  is a parametric variable describing the cylinder surface,

$$A_z^{(i)} = \int J_z(t') \frac{1}{4j} H_0^{(2)}(k_i R) dt' \quad (2.110)$$

$$\bar{F}_t^{(i)} = \int \hat{i}(t') K_t(t') \frac{1}{4j} H_0^{(2)}(k_i R) dt' \quad (2.111)$$

$$R = \sqrt{[x(t) - x(t')]^2 + [y(t) - y(t')]^2} \quad (2.112)$$

and  $\hat{i}$  is the unit vector tangent to the cylinder contour (Figure 2.26). The wavenumbers of the exterior medium and the dielectric region are denoted  $k_0$  and  $k_d$ , respectively; the intrinsic impedances of the exterior medium and the dielectric region are denoted  $\eta_0$  and  $\eta_d$ , respectively. The expressions in brackets in (2.108) and (2.109) differ depending on which side of the surface the observer is located. Equation (2.108) should be evaluated with the observer an infinitesimal distance *outside*  $S$ , while (2.109) should be evaluated with the observer an infinitesimal distance *inside*  $S$ .

In common with previous surface integral equation formulations, we assume that the cylinder model is represented by a superposition of flat strips, as illustrated in Figure 2.25. If pulse basis functions are used to represent the unknowns  $J_z$  and  $K_t$ , and Equations (2.108) and (2.109) are enforced in the center of each of the cells in the model, the result is a matrix equation having a  $2 \times 2$  block structure

$$\begin{bmatrix} \mathbf{E} \\ \mathbf{0} \end{bmatrix} = \begin{bmatrix} \mathbf{A} & \mathbf{B} \\ \mathbf{C} & \mathbf{D} \end{bmatrix} \begin{bmatrix} \mathbf{j} \\ \mathbf{k} \end{bmatrix} \quad (2.113)$$

where each entry in Equation (2.113) is an  $N \times N$  matrix having elements

$$A_{mn} = \frac{k_0\eta_0}{4} \int_{\text{cell } n} H_0^{(2)}(k_0 R) dt' \quad (2.114)$$

$$B_{mm} = \frac{1}{2} \quad (2.115)$$

$$B_{mn} = \frac{k_0}{4j} \int_{\text{cell } n} \left( \cos \phi_n \frac{\Delta x}{R_m} + \sin \phi_n \frac{\Delta y}{R_m} \right) H_1^{(2)}(k_0 R_m) dt' \quad m \neq n \quad (2.116)$$

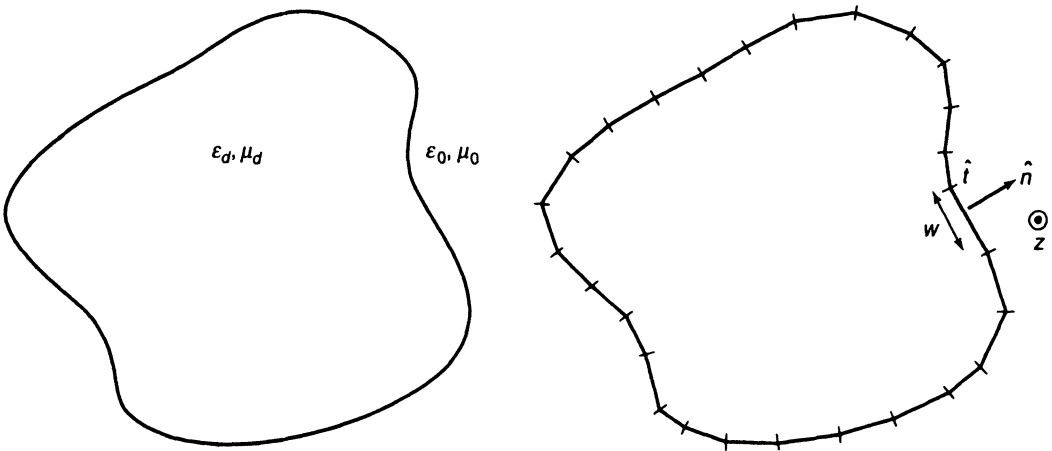


Figure 2.25 Flat-strip model of the surface of a homogeneous dielectric cylinder.

$$C_{mn} = \frac{k_d \eta_d}{4} \int_{\text{cell } n} H_0^{(2)}(k_d R) dt' \quad (2.117)$$

$$D_{mm} = -\frac{1}{2} \quad (2.118)$$

and

$$D_{mn} = \frac{k_d}{4j} \int_{\text{cell } n} \left( \cos \phi_n \frac{\Delta x}{R_m} + \sin \phi_n \frac{\Delta y}{R_m} \right) H_1^{(2)}(k_d R_m) dt' \quad m \neq n \quad (2.119)$$

where

$$\Delta x = x_m - x(t') \quad (2.120)$$

$$\Delta y = y_m - y(t') \quad (2.121)$$

$$R_m = \sqrt{(\Delta x)^2 + (\Delta y)^2} \quad (2.122)$$

and  $\phi_n$  is the polar angle defining the outward normal vector to the  $n$ th strip in the model, as illustrated in Figure 2.26. Expressions for  $B_{mm}$  and  $D_{mm}$  were obtained by a limiting procedure similar to that discussed in Section 2.2 and Prob. P2.8.

The data structure representing the cylinder model and the specific approach used to evaluate the expressions in (2.114)–(2.119) are generally identical to those used in previous surface integral equation formulations (Sections 2.1–2.2). The evaluation is slightly more complicated if the cylinder is lossy, in which case  $k_d$  is complex valued and the computations require a subroutine for Hankel functions of complex argument. Once these equivalent electric and magnetic sources are obtained by the solution of (2.113), the bistatic scattering cross section can be determined from

$$\sigma_{\text{TM}}(\phi) \cong \frac{k_0}{4} \left| \sum_{n=1}^N [\eta_0 j_n - k_n \cos(\phi - \phi_n)] w_n e^{jk_0(x_n \cos \phi + y_n \sin \phi)} \right|^2 \quad (2.123)$$

Fields within the dielectric cylinder (Prob. P2.30) can be obtained using source–field relationships that take the interior medium into account in conjunction with the sources  $J_z$  and  $K_t$  for the equivalent interior problem (which differ from the exterior sources obtained from the matrix solution by a  $180^\circ$  phase shift).

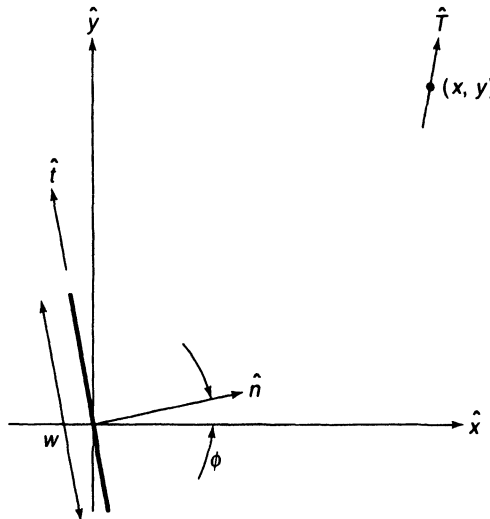


**Figure 2.26** Geometry of a source cell, showing normal and tangent vectors.

Coupled MFIEs describing the TE case can be formulated and discretized in a similar manner, and we leave this exercise to the reader (Prob. P2.31). We note in passing that, as an alternative formulation, coupled magnetic field equations can be developed for the TM polarization or coupled electric field equations can be used for the TE case.

We will illustrate the accuracy of the moment method formulation for the TE polarization based on coupled magnetic field equations (Prob. P2.31). Table 2.13 shows the magnitude and phase of the  $H_z$ -field within a circular, homogeneous cylinder having circumference of  $1\lambda_0$  and  $\epsilon_r = 2.56$ . These field values were computed as a secondary calculation after  $J_z$  and  $K_t$  were obtained from a 10-cell model and a 40-cell model (using equal-sized cells) of the circular contour. (This geometry was previously analyzed using the volume MFIE formulation of Section 2.7, with the results appearing in Figure 2.22.)

**TABLE 2.13**  $H_z$ -Field Along  $y = 0$  Cut through Circular, Homogeneous Cylinder with Circumference  $1\lambda_0$  and Relative Permittivity  $\epsilon_r = 2.56$  in Response to TE Plane Wave Propagating in  $\phi = 0$  Direction

$x(\lambda_0)$	H <sub>z</sub> -Field			H <sub>z</sub> -Field			
	N = 10	N = 40	Exact	N = 10	N = 40	Exact	
Magnitude				Phase (deg)			
-0.14	1.334	1.359	1.359	-130.51	-133.78	-134.05	
-0.10	1.502	1.507	1.509	-150.71	-151.31	-151.57	
-0.06	1.587	1.600	1.605	-166.63	-167.12	-167.37	
-0.02	1.600	1.623	1.630	177.79	177.49	177.29	
0.02	1.547	1.578	1.587	161.36	161.41	161.31	
0.06	1.453	1.486	1.496	143.08	143.66	143.69	
0.10	1.356	1.384	1.392	122.23	123.57	123.71	
0.14	1.291	1.309	1.314	96.03	101.28	101.60	

*Note:* A coupled MFIE formulation was used with  $N$  pulse basis functions and Dirac delta testing functions located on the surface of the dielectric cylinder; the fields within the cylinder were obtained as a secondary calculation. The exact solution is shown for comparison.

The numerical results produced by the surface integral equation exhibit good agreement with the exact solution and appear to improve as the number of basis functions is increased.

As a second example, the scattering cross section of a circular, homogeneous cylinder having circumference of  $0.248\lambda_0$  and  $\epsilon_r = 2 - j50$  is displayed in Table 2.14, where it is compared with data obtained from the volume EFIE formulation from Section 2.6 and the volume MFIE formulation from Section 2.7. Although the EFIE result is questionable (see Figure 2.18 and related discussion in Section 2.6), the volume MFIE and the surface MFIE results exhibit good agreement with the exact solution.

**TABLE 2.14** TE Bistatic Scattering Cross Section<sup>a</sup> of a Circular Cylinder with Circumference  $0.248\lambda_0$  and  $\epsilon_r = 2 - j50$  for Three Different Formulations

$\phi$ (deg)	Volume		Surface MFIE		
	EFIE 61 Cells, 122 Unknowns	MFIE 84 Cells, 55 Unknowns	10 Cells, 20 Unknowns	40 Cells, 80 Unknowns	Exact
0	-21.08	-22.37	-21.52	-22.24	-22.32
30	-22.29	-23.69	-22.81	-23.56	-23.64
60	-26.81	-28.70	-27.64	-28.55	-28.66
90	-41.31	-37.86	-38.41	-37.93	-37.70
120	-27.95	-26.78	-26.70	-26.74	-26.69
150	-23.13	-22.66	-22.39	-22.60	-22.58
180	-21.87	-21.53	-21.22	-21.47	-21.46

<sup>a</sup> In decibels free-space wavelength.

*Note:* Results from the volume EFIE approach from Section 2.6, the volume MFIE approach from Section 2.7, and the surface MFIE approach from this section are compared. The exact solution is shown for comparison.

Using the general principles discussed in Chapter 1, the surface integral equation formulation may be extended to treat scatterers made of several homogeneous regions. This topic is left as an exercise (Prob. P2.33).

## 2.9. INTEGRAL EQUATIONS FOR TWO-DIMENSIONAL SCATTERERS HAVING AN IMPEDANCE SURFACE

If the relative permittivity or permeability of a scatterer is large, an approximate impedance boundary condition (IBC) can sometimes be used to simplify the problem formulation beyond that of the coupled surface integral equations discussed in Section 2.8. If an IBC is valid, even inhomogeneous scatterers may be treated using a single surface integral equation instead of the volume formulations discussed previously.

Consider the scatterer illustrated in Figure 2.27. As discussed in Section 1.9, an equivalent exterior problem is obtained through the use of sources  $\bar{J}$  and  $\bar{K}$  defined on the surface of the original scatterer according to

$$\bar{J} = \hat{n} \times \bar{H} \quad (2.124)$$

$$\bar{K} = \bar{E} \times \hat{n} \quad (2.125)$$

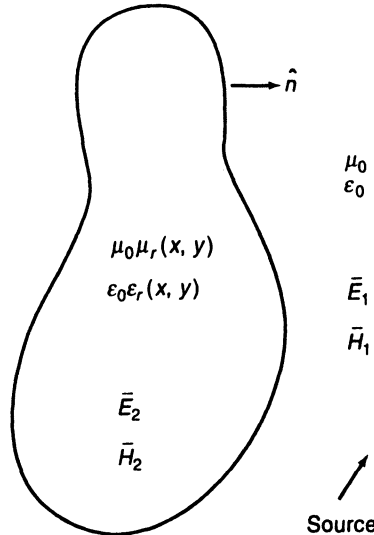


**Figure 2.27** Cross section of a general cylindrical scatterer.

and radiating in an infinite space having the same parameters as the exterior medium. If the scatterer material is such that a ray field impinging at any angle to the surface is transmitted at an internal angle very close to normal, the equivalent sources of (2.124) and (2.125) may satisfy the IBC [13]

$$\bar{K}(t) = \eta_s(t) \bar{J}(t) \times \hat{n}(t) \quad (2.126)$$

where  $\hat{n}$  is the outward normal vector to the surface and, in general, the surface impedance  $\eta_s$  of the scatterer may vary with location around the contour. In addition to the constraint mentioned above on the transmission direction of a ray field, in order for the IBC to be valid, sufficient loss must be present in the scatterer to ensure that the fields decay within the cylinder and do not emerge from the opposite side [14, 15].

Integral equations may be formulated in the usual manner to relate the incident electric or magnetic fields to the equivalent sources. In previous examples involving homogeneous dielectric bodies, the fact that both  $\bar{J}$  and  $\bar{K}$  were unknowns prompted the use of surface integral equations for both interior and exterior regions. If the impedance condition of Equation (2.126) is valid, it eliminates one of the two unknowns and the need to consider the interior region when formulating equations for penetrable bodies. As compared to a rigorous surface integral equation formulation, the IBC approach reduces the matrix order by a factor of 2. Since an impedance condition eliminates the need to find a Green's function for the interior region, its use permits a surface integral treatment of inhomogeneous bodies.

Consider a TM wave incident on a scatterer for which an impedance boundary condition is valid. Equivalent sources have components  $J_z$  and  $K_t$ , and the IBC reduces to

$$K_t(t) = E_z(t) = \eta_s(t) H_t(t) = \eta_s(t) J_z(t) \quad (2.127)$$

An electric field equation can be written entirely in terms of the equivalent electric current density  $J_z$  as

$$E_z^{\text{inc}}(t) = \eta_s(t) J_z(t) + jk\eta A_z + \left\{ \frac{\partial F_y}{\partial x} - \frac{\partial F_x}{\partial y} \right\}_{S^+} \quad (2.128)$$

where

$$A_z(t) = \int J_z(t') \frac{1}{4j} H_0^{(2)}(kR) dt' \quad (2.129)$$

$$\bar{F}_t(t) = \int \hat{i}(t') \eta_s(t') J_z(t') \frac{1}{4j} H_0^{(2)}(kR) dt' \quad (2.130)$$

and

$$R = \sqrt{[x(t) - x(t')]^2 + [y(t) - y(t')]^2} \quad (2.131)$$

The expression in brackets is to be evaluated an infinitesimal distance outside the surface.

For the case of a normally incident TE wave impinging on a scatterer that can be represented using an IBC, equivalent sources have components  $J_t$  and  $K_z$ . The impedance condition is given by

$$K_z(t) = -E_t(t) = \eta_s(t) H_z(t) = -\eta_s(t) J_t(t) \quad (2.132)$$

A TE EFIE can be written entirely in terms of the equivalent electric current density  $J_t$  according to

$$E_t^{\text{inc}}(t) = \eta_s(t) J_t(t) - \left\{ \hat{i} \cdot \frac{\nabla \nabla \cdot + k^2}{j\omega\epsilon} \bar{A}_t \right\} + \{\hat{i} \cdot \nabla \times \bar{F}_z\}_{S^+} \quad (2.133)$$

where

$$\bar{A}_t(t) = \int \hat{i}(t') J_t(t') \frac{1}{4j} H_0^{(2)}(kR) dt' \quad (2.134)$$

$$F_z(t) = - \int \eta_s(t') J_t(t') \frac{1}{4j} H_0^{(2)}(kR) dt' \quad (2.135)$$

and  $R$  is defined in Equation (2.131). As an alternative, a TE MFIE can be written in terms of  $J_t$  as

$$H_z^{\text{inc}}(t) = -J_t(t) - \{\hat{z} \cdot \nabla \times \bar{A}_t\}_{S^+} + j\omega\epsilon F_z \quad (2.136)$$

In either of these equations, the subscript  $S^+$  indicates that the bracketed term is to be evaluated an infinitesimal distance outside the scatterer surface.

For either polarization, the discretization of these integral equations into matrix form can be carried out following a procedure similar to that of previous examples. Issues such as the model used to represent the cylinder surface, the basis and testing functions, and the algorithm employed to evaluate the required integrals have been discussed in Sections 2.1, 2.2, and 2.4. Thus, we omit further details of the implementation.

To illustrate the use of an impedance boundary condition, consider the triangular dielectric cylinder depicted in Figure 2.28. We will limit ourselves to the TE polarization. This cylinder has perimeter equal to  $3.24\lambda_0$  and relative permittivity  $\epsilon_r = 20 - j50$ . Although the material appears to be compatible with an impedance boundary condition, the small size of the scatterer and the presence of sharp corners may invalidate the IBC approximation.

In order to investigate the validity of the IBC, we first treat this scatterer using the rigorous surface integral equation formulation from Section 2.8 (Prob. P2.31) for a 55-cell model and pulse basis functions for both  $J_t$  and  $K_z$ . Once the coefficients of the basis functions have been determined by a solution of the matrix equation, the ratio of  $K_z$  to  $J_t$  can be examined in order to justify the impedance concept. Tables 2.15 and 2.16 show this ratio for the equivalent currents on the top and back sides of the triangular cylinder. The

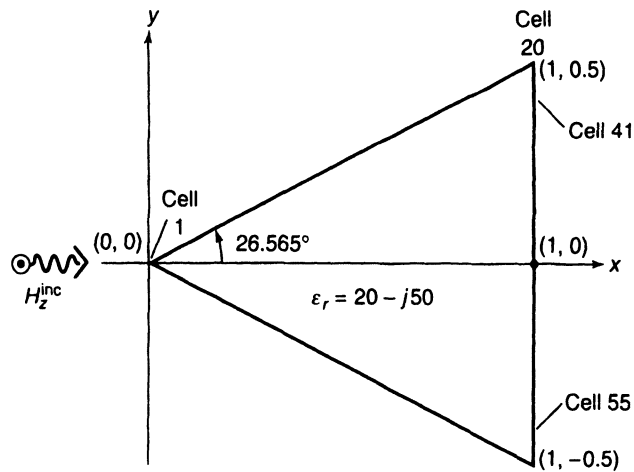


**Figure 2.28** Cross section of a triangular dielectric cylinder. The coordinate locations are in units of free-space wavelength.

**TABLE 2.15** Ratio of  $-K_z$  to  $J_t$  Along Lit Face of Homogeneous, Triangular Dielectric Cylinder with  $\epsilon_r = 20 - j50$  Produced by Pulse Basis/Delta Testing Discretization of Coupled MFIE from Section 2.8

Cell Number	Magnitude	Phase (deg)
1	31.839	69.32
2	57.125	46.37
3	52.003	38.51
4	49.546	39.97
5	49.926	40.82
6	50.118	40.67
7	50.064	40.59
8	50.037	40.59
9	50.042	40.59
10	50.050	40.58
11	50.061	40.58
12	50.070	40.60
13	50.068	40.62
14	50.052	40.64
15	50.015	40.65
16	50.014	40.60
17	50.062	40.77
18	49.299	40.60
19	51.040	37.85
20	52.751	47.53

*Note:* The ratio should be compared with the intrinsic impedance of the dielectric material, which in this case has a magnitude equal to  $51.34 \Omega$  and a phase angle of  $34.1^\circ$ .

**TABLE 2.16** Ratio of  $-K_z$  to  $J$ , Along Back Wall of Homogeneous, Triangular Dielectric Cylinder with  $\epsilon_r = 20 - j50$  Produced by Pulse Basis/Delta Testing Discretization of Coupled MFIE from Section 2.8

Cell Number	Magnitude	Phase (deg)
41	2.873	116.83
42	52.832	52.14
43	49.384	40.65
44	46.074	41.97
45	46.717	42.23
46	47.343	42.62
47	47.402	42.63
48	47.404	42.64
49	47.402	42.63
50	47.344	42.62
51	46.717	42.23
52	46.074	41.97
53	49.384	40.65
54	52.832	52.14
55	2.873	116.83

*Source:* The ratio should be compared with the intrinsic impedance of the dielectric material, which in this case has a magnitude equal to  $51.34 \Omega$  and a phase angle of  $34.1^\circ$ .

numerical values in these tables support the use of an IBC but suggest a surface impedance of approximately  $38 + j33\Omega$  for the lit face and  $35 + j32\Omega$  for the back face of the cylinder. The intrinsic impedance of this material is  $42.51 + j28.78\Omega$ , which differs from these values by 12 and 16%, respectively. Despite the difference, the scattering cross section obtained from a TE MFIE code incorporating the IBC with  $\eta_s = 42.51 + j28.78\Omega$  exhibits reasonable agreement with the result from the rigorous coupled MFIE formulation (Table 2.17). Both

**TABLE 2.17** Bistatic Scattering Cross Section  $\sigma_{TE}$  of Triangular Dielectric Cylinder Having  $\epsilon_r = 20 - j50$

$\phi$	MFIE with IBC	Coupled MFIE
0	7.20	7.13
30	3.39	3.34
60	2.35	2.99
90	-5.14	-4.70
120	-15.56	-15.83
150	-11.46	-11.49
180	-9.25	-9.54

*Note:* In decibels free-space wavelength.  
Comparison of numerical results obtained using an (IBC) of  $\eta_s = 42.51 + j28.78$  within an MFIE formulation and a rigorous coupled surface MFIE formulation. Results are based on the identical 55-cell model.

procedures use pulse basis functions and Dirac delta testing functions and a 55-cell model of the cylinder contour.

## 2.10. SUMMARY

Throughout this chapter, procedures were presented for the numerical solution of a variety of integral equations representing two-dimensional scattering geometries. Both surface integral equations and volume integral equations were considered, since the discretization process is similar in both cases. In an attempt to maintain an introductory level of presentation, the methods discussed are among the simplest that appear to produce accurate, converging results. We also discussed some procedures that do not always work well in an attempt to understand why these techniques fail. Throughout, we tried to provide enough detail in order to facilitate a computer implementation. Appendices C and D describe sample FORTRAN codes that demonstrate these techniques.

We have deferred a number of interesting topics to later chapters. Chapter 4 addresses common matrix solution algorithms and considers the effect of the stability of the matrix equation. Chapter 5 presents a theoretical examination of the discretization process and attempts to address the question of convergence. Alternative surface integral equation formulations are considered in Chapter 6, where difficulties that arise in several special situations are investigated. Chapter 7 presents an extension of the present formulations to geometries with one-dimensional periodicity. Chapter 8 considers the case of waves incident on infinite cylinders from oblique angles with respect to the cylinder axis, which is a building block needed to treat a finite source radiating in the presence of an infinite cylinder. We have mentioned that smoother basis and testing functions should provide improved accuracy, and a variety of examples of alternative basis and testing functions are presented in Chapter 9. Chapter 9 also introduces the use of curved-cell models. Finally, the development of integral equation formulations for three-dimensional scatterers is treated in Chapter 10.

Integral equations encompass only one of several different ways of posing an electromagnetic scattering problem. In the following chapter, alternative formulations are considered that employ a direct discretization of the scalar Helmholtz equations for two-dimensional scattering. These procedures may be more efficient for heterogeneous scatterers than the volume integral equation formulations discussed in the present chapter.

## REFERENCES

- [1] R. F. Harrington, *Field Computation by Moment Methods*, Malabar, FL: Krieger, 1982.
- [2] M. Abramowitz and I. A. Stegun, *Handbook of Mathematical Functions*, New York: Dover, 1965.
- [3] D. R. Wilton and C. M. Butler, "Effective methods for solving integral and integro-differential equations," *Electromagnetics*, vol. 1, pp. 289–308, 1981.
- [4] A. W. Glisson and D. R. Wilton, "Simple and efficient methods for problems of electromagnetic radiation and scattering from surfaces," *IEEE Trans. Antennas Propagat.*, vol. AP-28, pp. 593–603, Sept. 1980.

- [5] J. H. Richmond, "Scattering by a dielectric cylinder of arbitrary cross section shape," *IEEE Trans. Antennas Propagat.*, vol. AP-13, pp. 334–341, May 1965.
- [6] I. S. Gradshteyn and I. M. Ryzhik, *Table of Integrals, Series, and Products*, New York: Academic, 1980.
- [7] O. M. Al-Bundak, "Electromagnetic scattering of arbitrarily shaped inhomogeneous cylinders whose cross-sections are modeled by triangular patches," M.S. thesis, University of Mississippi, University, MS, 1983.
- [8] J. H. Richmond, "TE-wave scattering by a dielectric cylinder of arbitrary cross section shape," *IEEE Trans. Antennas Propagat.*, vol. AP-14, pp. 460–464, July 1966.
- [9] M. J. Hagmann and R. L. Levin, "Criteria for accurate usage of block models," *J. Microwave Power*, vol. 22, pp. 19–27, Jan. 1987.
- [10] D. T. Borup, D. M. Sullivan, and O. P. Gandhi, "Comparison of the FFT conjugate gradient method and the finite-difference time domain method for the 2-D absorption problem," *IEEE Trans. Microwave Theory Tech.*, vol. MTT-35, pp. 383–395, Apr. 1987.
- [11] A. F. Peterson and P. W. Klock, "An improved MFIE formulation for TE-wave scattering from lossy, inhomogeneous dielectric cylinders," *IEEE Trans. Antennas Propagat.*, vol. AP-36, pp. 45–49, Jan. 1988.
- [12] T. K. Wu and L. L. Tsai, "Scattering by arbitrarily cross sectioned layered lossy dielectric cylinders," *IEEE Trans. Antennas Propagat.*, vol. AP-25, pp. 518–524, July 1977.
- [13] K. M. Mitzner, "An integral equation approach to scattering from a body of finite conductivity," *Radio Science*, vol. 2, pp. 1459–1470, Dec. 1967.
- [14] D. S. Wang, "Limits and validity of the impedance boundary condition," *IEEE Trans. Antennas Propagat.*, vol. AP-35, pp. 453–457, Apr. 1987.
- [15] S. W. Lee and W. Gee, "How good is the impedance boundary condition?" *IEEE Trans. Antennas Propagat.*, vol. AP-35, pp. 1313–1315, Nov. 1987.

## PROBLEMS

**P2.1** (a) Consider the matrix operator arising in the TM EFIE formulation of Section 2.1. Under what conditions is the matrix in (2.7) symmetric ( $Z_{mn} = Z_{nm}$ )? Propose a simple way of modifying the formulation to always ensure symmetry.

(b) Other types of matrix symmetry appear in special cases. A matrix with  $Z_{mn} = Z_{m-n}$  is a Toeplitz matrix, which appears in the form

$$\begin{bmatrix} z_0 & z_1 & z_2 & & \\ z_1 & z_0 & z_1 & \cdots & \\ z_2 & z_1 & z_0 & & \\ \vdots & & & & \\ \vdots & & & & \end{bmatrix}$$

in the symmetric case. Identify two different scatterer geometries that, when used with equal-sized cells, cause Equation (2.7) to exhibit the Toeplitz structure.

**P2.2** The worst-case error in Equation (2.10) occurs when the source and observation cells are closely spaced. To study this error, consider the formulation of Section 2.1 applied

to TM scattering from a flat p.e.c. strip. If the cell sizes are restricted to width  $w$ , the matrix entry immediately adjacent to the main diagonal is given by

$$Z_{12} = \frac{k\eta}{4} \int_{w/2}^{3w/2} H_0^{(2)}(kx) dx$$

According to Equation (2.10), this expression may be approximated by

$$Z_{12}^{\text{app}} = \frac{k\eta w}{4} H_0^{(2)}(kw)$$

Using

$$H_0^{(2)}(kx) \cong 1 - j \frac{2}{\pi} \ln\left(\frac{\gamma kx}{2}\right) \quad \text{as } kx \rightarrow 0$$

show that

$$\frac{Z_{12} - Z_{12}^{\text{app}}}{Z_{12}} \cong \frac{-j(2/\pi) \ln(3\sqrt{3}/2e)}{1 - j(2/\pi) \ln[(\gamma kw/2)(3\sqrt{3}/2e)]}$$

as  $w \rightarrow 0$ . What does this result suggest about the approximation in (2.10)?

- P2.3** (a) Data from Table 2.1 suggest that the approximation of Equation (2.10) produces an error in the plane of the source cell that is independent of the distance to the observer for large separations. It is conjectured that this error is due to the phase cancellation ignored by the single-point approximation. Since  $R \cong \rho - x' \cos \phi - y' \sin \phi$  as  $\rho \rightarrow \infty$ , integrate over the asymptotic form

$$H_0^{(2)}(kR) \approx \sqrt{\frac{2j}{\pi k\rho}} e^{-jkR} \quad \text{as } \rho \rightarrow \infty$$

in order to derive the “improved” approximation

$$\int_{-w/2}^{w/2} \frac{1}{4j} H_0^{(2)}(k|x - x'|) dx' \cong \frac{1}{4j} H_0^{(2)}(kw) \frac{2}{k} \sin\left(\frac{kw}{2}\right)$$

- (b) Using numerical data from Table 2.1, tabulate the error in this improved expression for  $w = 0.1$  and  $k = 2\pi$ .
- (c) Generalize this approximation to obtain a formula valid for all orientations of the source strip with respect to the observation point.
- P2.4** Using the computer program described in Appendix A for TM scattering from p.e.c. cylinders, find the surface currents and scattering cross section for circular cylinders of circumference  $1.0\lambda_0$ ,  $2.0\lambda_0$ , and  $2.405\lambda_0$ . If possible, compare your numerical results with exact solutions. Do the results seem to converge in every case with an increasing number of cells in the models? Based on your observations, propose guidelines for minimum cell densities.

- P2.5** The formulation for TM scattering from p.e.c. cylinders can be improved by replacing Equation (2.10) with an evaluation of (2.8) by numerical quadrature. Assume that we retain the flat-cell model, the pulse basis functions, and the Dirac delta testing functions but extend the original approach to include the orientation of cells. Provide a detailed expression for the integrand as a function of the integration variable  $t'$  along the source cell. Discuss the impact of this change on the required scatterer model and the computational overhead.

**P2.6** At the tip of a p.e.c. wedge with interior angle  $\Omega$  (Figure 2.29), the TM current density is known to behave according to

$$J_z \approx \rho^{-(\pi-\Omega)/(2\pi-\Omega)} \quad \text{as } \rho \rightarrow 0$$

if  $\rho$  is the distance from the tip (N. Morita, N. Kumagai, and J. R. Mautz, *Integral Equation Methods for Electromagnetics*, Boston: Artech House, 1990). Basis functions used to represent  $J_z$  at the tip can be modified to incorporate this singularity for  $0 \leq \Omega < \pi$ . Propose at least one way of modifying the piecewise-constant basis functions used in Section 2.1 to obtain a new function with a singularity of the proper order at one edge of a cell.

**P2.7** Data in Table 2.2 suggest that the error in the TM current density is proportional to  $O(\Delta)$  as  $\Delta \rightarrow 0$ , where  $\Delta$  is the cell size. Given such knowledge, two successive results can be used to extrapolate to a more accurate value. For instance, if  $J_N$  is the numerical value obtained for the current density using  $N$  cells of uniform width  $\Delta_N$ , then the dominant error in the current density is roughly  $K\Delta_N$ , and we can write

$$J_\infty \cong J_N + K\Delta_N$$

where  $J_\infty$  is the exact result. It follows that by doubling the number of cells we obtain a new result  $J_{2N}$  satisfying

$$J_\infty \cong J_{2N} + K(\Delta_N/2)$$

These two equations can be combined to eliminate  $K$  and produce

$$J_\infty \cong 2J_{2N} - J_N$$

which should be a more accurate result than either  $J_N$  or  $J_{2N}$ . This procedure is a special case of *Richardson extrapolation* (K. E. Atkinson, *An Introduction to Numerical Analysis*, New York: Wiley, 1989).

Use the values in Table 2.2 for  $N = 32$  and  $N = 64$  to extrapolate to a more accurate result for the current density. What is the percentage error in the extrapolated value in each case? Is the extrapolation process more efficient than using additional unknowns?

**P2.8** (a) Show that the  $H_z$ -field due to a current density

$$\tilde{J}_t(t) = \hat{y}p(y; -a, a)\delta(x)$$

radiating in free space is given at a point  $(x, 0)$  by the expression

$$H_z^s(x, 0) = \frac{\partial A_y}{\partial x} = -\frac{k}{4j} \int_{y'=-a}^a \frac{x}{R} H_1^{(2)}(kR) dy'$$

where

$$R = \sqrt{x^2 + (y')^2}$$

(b) Using the approximation

$$H_1^{(2)}(kR) \cong \frac{kR}{2} + j \frac{2}{\pi kR} \quad \text{as } kR \rightarrow 0$$

evaluate the integral to show that

$$\lim_{x \rightarrow 0} H_z^s(x, 0) = \begin{cases} -\frac{1}{2} & x > 0 \\ +\frac{1}{2} & x < 0 \end{cases}$$

This completes the derivation of Equation (2.29).

- (c) Although this derivation has been carried out for the two-dimensional case, the result can be extended to produce the scattered magnetic field an infinitesimal distance from an electric source on a smooth surface in three dimensions. Explain the equivalence.

**P2.9** Following the basic procedure presented for the TE polarization in Section 2.2, develop a tangential-field MFIE formulation for TM scattering from closed, perfectly conducting cylinders.

- Identify the field components and current components present, and specialize Equation (1.97) to the two-dimensional TM case.
- Introduce pulse basis functions and Dirac delta testing functions in order to discretize the MFIE into matrix form. Provide expressions for the diagonal and off-diagonal matrix entries (the off-diagonal entries may be left in the form of an integral, but use a limiting process analogous to that of Prob. P2.8 to obtain the diagonal entries) as well as the entries of the excitation vector.
- Describe the minimum data structure required to represent the cylinder geometry.

**P2.10** Generalize Prob. P2.8 in order to obtain the scattered  $H_z$ -field at the tip of a wedge produced by a uniform transverse current density  $J_t$ , as depicted in Figure 2.29. Show that  $H_z^s$  is given by

$$\lim_{x \rightarrow 0} H_z^s(x, 0) = -\frac{\Omega}{2\pi}$$

[Hint: You should obtain

$$H_z^s(x, 0) = -\frac{x \sin(\Omega/2)}{\pi} \int_{t'=0}^w \frac{dt'}{x^2 + 2xt' \cos(\Omega/2) + (t')^2}$$

as an intermediate result.]

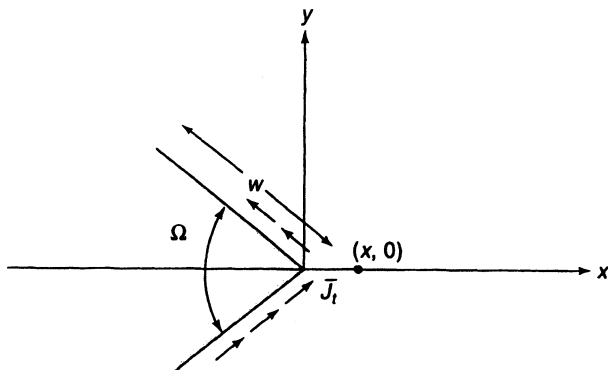


**Figure 2.29** Geometry of a p.e.c. wedge (for Prob. P2.6).

**P2.11** Using the result of Prob. P2.10, develop a TE MFIE formulation for closed p.e.c. scatterers based on subsectional triangle basis functions for  $J_t$  and Dirac delta testing functions. The basis and testing functions are to be centered at the edges of flat cells comprising the model, so that the triangle functions overlap two adjacent cells. Provide detailed expressions for the matrix entries (diagonal and off-diagonal cases) under the assumption that numerical quadrature will be used to evaluate the off-diagonal entries. Describe the minimum data structure necessary to represent the cylinder geometry.

- P2.12** The MFIE of (2.19) is enforced an infinitesimal distance *outside* the scatterer surface. Using concepts from Sections 1.6 and 1.7 and the result of Prob. P2.8, develop an equivalent TE MFIE expressed an infinitesimal distance *inside* the surface. Evaluate the diagonal matrix entries that would arise from a numerical discretization analogous to that used in Section 2.2. Explain any differences between the original MFIE and this equation.
- P2.13** Develop a TE implementation of the normal-field MFIE introduced in Prob. P1.19 by treating the transverse current density as the primary unknown and employing pulse basis functions and Dirac delta testing functions defined on flat cells. Provide expressions for the diagonal and off-diagonal matrix entries and the entries of the excitation vector. Compare the normal-field formulation to the approach discussed in Section 2.2. Can you identify any advantages or disadvantages?
- P2.14** Equation (2.33) was obtained by specializing (1.52) to produce the  $x$ -component of the electric field due to a two-dimensional  $x$ -directed current density. Generalize this result to obtain an expression for the  $y$ -component of the electric field produced by the current in Equation (2.34). By combining your result with (2.38), provide the complete expression for the electric field due to the current density.
- P2.15** Develop a FORTRAN subroutine to compute the scattering cross section according to Equation (2.59) for the TE EFIE approach of Section 2.4. Assume that the input data consists of a cylinder model (Figure 2.11 and Table 2.9) and the coefficients  $\{j_n\}$  determined by the prior solution of Equation (2.51).
- P2.16** The TE EFIE formulation of Section 2.4 can be extended to treat junctions between strips and closed cylinders. For a junction between three cells, develop a scheme for placing basis and testing functions that satisfies Kirchhoff's current law at the junction. How does the TE situation differ from the TM approach presented in Section 2.1?
- P2.17** Using the subroutine (Appendix D) for the entries of Equation (2.51), generate a FORTRAN program to implement the TE EFIE formulation for p.e.c. strips and cylinders discussed in Section 2.4. You may assume that a suitable cylinder model has been placed in an input data file in the form described in Table 2.9 (a list of nodes, a pointer from cell indices to adjacent node indices, and a second pointer from basis function locations to the adjacent cell indices). You may also neglect the treatment of junctions between multiple strips. Develop sections of code to read the cylinder model from the data file, fill the matrix equation, create the excitation vector for an incident field of the form

$$H_z^{\text{inc}}(x, y) = e^{-jk(x \cos \theta + y \sin \theta)}$$

solve the matrix equation, and write the coefficients of the basis functions to an output file. Test your program by comparing results for circular cylinders with exact solutions. Study the convergence of the numerical solutions as a function of the number of cells used in the model (i.e., try 5 cells/ $\lambda$ , 10 cells/ $\lambda$ , etc.).

- P2.18** Study the accuracy of the approximation employed in Equation (2.56) for the special case when the basis and testing functions are located on a common plane by developing software that provides an accurate evaluation of the double integral required in (2.53). Tabulate the error in the approximation as a function of displacement between the source cell and the observation cell for cell sizes of  $w = 0.1\lambda_0$  and  $w = 0.05\lambda_0$ .
- P2.19** Verify the integral presented in Equation (2.71).
- P2.20** An analytical result is obtained in Equation (2.72) for the off-diagonal matrix entries associated with the TM EFIE formulation of Section 2.5. Compare this expression with the obvious single-point approximation to the integral, that is,

$$Z_{mn} \cong \frac{k\eta}{4}\pi a_n^2 H_0^{(2)}(kR_{mn})$$

Would an improved single-point approximation similar to that introduced in Prob. P2.3 be likely to enhance the accuracy of (2.72)?

- P2.21** The volume integral formulation of Section 2.5 for TM scattering from dielectric cylinders employed  $J_z$  instead of  $E_z$  as the primary unknown to be determined. Formulate a matrix equation similar to (2.67) based on  $E_z$  as the primary unknown. Compare the two approaches and identify the differences. Can you think of an advantage of one formulation over the other?

- P2.22** Reformulate the EFIE discretization presented for TM-wave scattering from dielectric cylinders in Section 2.5 in order to replace the square cells with triangular cells.

- Provide integral expressions for the diagonal and off-diagonal matrix entries obtained using pulse basis functions and Dirac delta testing functions (assume that a quadrature algorithm will be employed to evaluate integrals over triangular domains).
- Develop a procedure for evaluating the diagonal matrix entries, which are complicated by the singularity in the Hankel function.
- Develop a data structure to represent the triangular-cell scatterer geometry. How does the minimum model compare with that required in Section 2.5?

- P2.23** The problem of a TE wave incident on an inhomogeneous magnetic (permeable) cylinder is the electromagnetic “dual” to that of a TM wave incident on a dielectric cylinder (duality is reviewed in Section 1.5). Based on the EFIE formulation of Section 2.5, develop an MFIE formulation for the TE magnetic cylinder problem, assuming that the discretization employs pulse basis functions and Dirac delta testing functions on square cells. Treat the magnetic polarization current density

$$K_z(x, y) = j\omega\mu_0[\mu_r(x, y) - 1]H_z(x, y)$$

as the primary unknown. Provide expressions for the matrix entries using approximations analogous to those employed in Section 2.5.

- P2.24** By combining the essential features of the formulations described in Sections 2.1 and 2.5, develop a procedure for TM scattering from composite cylinders containing p.e.c. and dielectric materials. Describe the matrix equation and provide expressions for the matrix entries. What features of this approach make the matrix entries so easy to obtain?

- P2.25** By employing the “circular-cell” approximation introduced in Equation (2.71), evaluate Equations (2.89)–(2.93) to obtain analytical expressions.

- P2.26** (a) Derive Equations (2.101) and (2.102).  
(b) With the help of Maxwell’s equations, show that the use of a continuous expansion for  $H_z$  in Section 2.7 guarantees the proper continuity of the normal component of the electric field at a cell interface and therefore eliminates fictitious charge density.

- P2.27** An edge located between two cells is depicted in Figure 2.21. If the tangent vector along the edge is defined in terms of the angle  $\Omega$  by

$$\hat{t}(t) = \hat{x} \cos \Omega(t) + \hat{y} \sin \Omega(t)$$

develop explicit expressions for the parameters  $\{\alpha_n\}$  appearing in Equation (2.105) as a function of  $\Omega$ , the relative permittivity  $\epsilon_r$  of the two adjacent cells, and the coordinates  $(x_n, y_n)$  of the surrounding nodes.

- P2.28** Extend Prob. P2.22 to produce a volume EFIE formulation for TM scattering from dielectric cylinders based on a linear pyramid representation of the internal  $E_z$ -field. Provide expressions for the matrix entries obtained using pyramid basis functions and Dirac delta testing functions centered at the corners of triangular cells. Develop a

procedure for evaluating the diagonal matrix entries in order to treat the singularity when the testing function location coincides with a source cell. Propose a data structure to represent the triangular-cell model.

- P2.29** By combining the TM EFIE formulation from Prob. P2.28 with the electromagnetic dual of the MFIE formulation described in Section 2.7, develop a triangular-cell EFIE formulation for TM scattering from cylinders having dielectric and magnetic inhomogeneities. In this formulation, both electric polarization currents and magnetic polarization currents can be simultaneously defined in terms of the  $E_z$ -field using

$$J_i(x, y) = j\omega\epsilon_0[\epsilon_r(x, y) - 1]E_i(x, y)$$

$$\bar{K}(x, y) = -\frac{\mu_r(x, y) - 1}{\mu_r(x, y)} \nabla \times \bar{E}_z$$

Provide expressions for the matrix entries arising from a linear pyramid representation for  $E_z$  and point matching at the corners of triangular cells.

- P2.30** The integral formulation of Section 2.8 produces a numerical solution for the tangential fields on the surface of a homogeneous cylinder. The internal fields can be found from a secondary calculation by treating the surface fields as equivalent sources. For the TM polarization, provide expressions for the internal  $E_z$ -field and the internal  $H_x$ - and  $H_y$ -fields at an arbitrary point within a homogeneous cylinder of permittivity  $\epsilon_d$  and permeability  $\mu_d$  as a function of the tangential fields  $E_z(t)$  and  $H_t(t)$  on the cylinder surface.

- P2.31** Using electromagnetic duality (Section 1.5), formulate an MFIE approach for TE scattering from a homogeneous dielectric cylinder that parallels the TM formulation discussed in Section 2.8. Provide all the matrix entries.

- P2.32** A volume discretization requires unknowns distributed throughout the interior of the geometry under consideration, whereas surface integral equations confine the unknowns to the scatterer surface. For a homogeneous dielectric cylinder having radius  $a = 50\lambda_0$  and relative permittivity  $\epsilon_r = 10$ , estimate the number of unknowns required with the volume integral formulation of Section 2.5 and the surface integral formulation of Section 2.8. Assume that a density of  $100 \text{ cells}/\lambda_d^2$  is required for the volume approach and  $10 \text{ cells}/\lambda_d$  is required for the surface approach.

- P2.33** Specialize the coupled EFIE formulation developed in Prob. P1.20 for a layered dielectric scatterer to the two-dimensional TM case. Using pulse basis functions and Dirac delta testing functions, convert the resulting equations into matrix form. Show that the matrix structure has the form

$$\begin{bmatrix} X & X \\ X & X & X & X \\ X & X & X & X \\ & X & X \end{bmatrix} \begin{bmatrix} J_1 \\ K_1 \\ J_2 \\ K_2 \end{bmatrix} = \begin{bmatrix} E_{S_1^+}^{\text{inc}} \\ 0 \\ 0 \\ 0 \end{bmatrix}$$

Extend this result to the case of a core dielectric region surrounded by two layers of homogeneous material. In that case, you should obtain a matrix having the structure

$$\begin{bmatrix} X & X \\ X & X & X & X \\ X & X & X & X \\ & X & X & X & X \\ X & X & X & X \\ & X & X \end{bmatrix} \begin{bmatrix} J_1 \\ K_1 \\ J_2 \\ K_2 \\ J_3 \\ K_3 \end{bmatrix} = \begin{bmatrix} E_{S_1^+}^{\text{inc}} \\ 0 \\ 0 \\ 0 \\ 0 \\ 0 \end{bmatrix}$$

Does the structure present in these systems suggest a recursive elimination procedure?

Outline such a process, and comment on the savings possible for a scatterer containing a large number of thin layers of homogeneous material.

- P2.34** Develop expressions for the matrix entries associated with a discretization of Equation (2.128) employing pulse basis functions and Dirac delta testing functions.
- P2.35** Discuss the discretization of Equation (2.133). What basis and testing functions should be used to compensate for the additional derivatives?
- P2.36** A thin absorber known as a “resistive card” can be modeled as a shell of lossy dielectric material. If the shell has thickness  $\Delta$ , where  $\Delta$  is small compared with the wavelength, the relationship

$$\bar{J} = j\omega\epsilon_0(\epsilon_r - 1)\bar{E}$$

between the volume current density and the electric field can be used to obtain the approximate boundary condition

$$\bar{E}_{\tan} = \frac{\Delta}{j\omega\epsilon_0(\epsilon_r - 1)} \bar{J}_{\tan} = R_s \bar{J}_{\tan}$$

where  $\bar{J}_{\tan}$  is an equivalent surface current density and  $R_s$  is the resistance of the card. Observe that a p.e.c. surface may be modeled by  $R_s = 0$ . Reformulate the TM EFIE formulation of Section 2.1 in order to incorporate this boundary condition. What changes are necessary in the matrix entries?

- P2.37** Incorporate the resistive boundary condition from Prob. P2.36 into the TE EFIE formulation presented in Section 2.4. Describe any alterations in the entries of the moment method impedance matrix.